# We are IntechOpen,
the world's leading publisher of
Open Access books
Built by scientists, for scientists

## 4,800
Open access books available

## 122,000
International authors and editors

## 135M
Downloads

Our authors are among the

## 154
Countries delivered to

## TOP 1%
most cited scientists

## 12.2%
Contributors from top 500 universities

CLARIVATE ANALYTICS
BOOK CITATION INDEX
INDEXED

**WEB OF SCIENCE**™

Selection of our books indexed in the Book Citation Index
in Web of Science™ Core Collection (BKCI)

## Interested in publishing with us?
Contact book.department@intechopen.com

# Inversion of Amplitude from the 2-D Analytic Signal of Self-Potential Anomalies

Arkoprovo Biswas

Additional information is available at the end of the chapter

## Abstract

In the present study, analytic signal amplitude (ASA) or total gradient (TG) inversion of self-potential anomalies has been carried out using very fast simulated annealing (VFSA) global optimization technique. The results of VFSA optimization demonstrate the application and efficacy of the proposed method for idealized synthetic hypothetical models and real single and multiple geological structures. The model parameters deciphered here are the amplitude coefficient ($k$), horizontal location ($x_0$), depth of the body ($z$), and shape ($q$). Inversion of the model parameter suggests that constraining the horizontal location and the shape factor offers the most reliable results. Investigation of convergence rate, histogram, and cross-plot examination suggest that the interpretation method developed for the self-potential anomalies is stable and the model parameters are within the estimated ambiguity. Inversion of synthetic noise-free and noise-corrupted data for single structures and multiple structures in addition to real field information exhibits the viability of the method. The model parameters estimated by the present technique were in good agreement with the real parameters. The method has been used to invert two field examples (Sulleymonkoy anomaly, Ergani, Turkey, Senneterre area of Quebec, Canada) with application of subsurface mineralized bodies. This technique can be very much helpful for mineral or ore bodies investigation of idealized geobodies buried within the shallow and deeper subsurface.

**Keywords:** self-potential, total gradient, idealized bodies, VFSA, uncertainty estimation, ore exploration

## 1. Introduction

The self-potential (SP) technique has an important significance in mineral and ore explorations [1–8]. The method has an extensive range of application, viz., mining industries [9–12], sulfide, graphite exploration, and groundwater exploration [13, 14], study of groundwater

flow in pumping wells [15, 16], geothermal exploration [17–19], fluid flow in the vadose zone [20, 21], uranium mineralization [2–4], engineering and environmental applications [22–24], archeological investigations [25], cave detection [26], earthquake prediction [27], hydraulic fracturing [28], brine contamination [29], spring flow [30], delineation of buried paleochannels [31], volcanic eruptions [32, 33], and paleoshear zones [34].

In general, most of the interpretation of SP anomaly is carried out assuming simple geometrical shapes (for example, 3-D sphere, 2-D horizontal or vertical cylinder, and 2-D sheet) buried at variable depth generated by different mineral or ore bodies [2, 3, 7, 34–47]. Numerous interpretation techniques have been developed over the last two decades considering various interpretation methods [38, 40, 48–53]. For instance, graphical methods [42, 54], the nomograms [42], logarithmic curve matching [41, 55], characteristic points, [43, 45, 56], least square method [38, 57], Fourier analysis [58], 3-D topography effect [59, 60], gradient and derivative study [61], moving average residual anomalies [62], modular neural networks [49], particle swarm optimization [63], depth from extreme point [64], differential evolution [65], Genetic-Price algorithm [66], spectral and tomographic approach [67], second horizontal gradient [68], and spectral methods [69] were too applied for the elucidation of SP data. A detailed review of the SP background, theoretical modeling, inversion, and its application in mineral exploration can be found after Biswas [1].

Among various interpretation and inversion techniques mentioned above, for the most part, inverse modeling intends to do the best interpretation of the model parameters. It is very familiar in geophysical data that the nonuniqueness problem, nonlinearity, and ill-posed nature of the SP anomaly inversion make the processing and elucidation rather cumbersome. Also, in linear problems for SP data, the presence of less number of well-known numbers rather than the number of unidentified geological model parameters often shows an uncertainty, which creates the interpretation quite difficult [70]. Subsequently, the inversion problems of SP anomaly firmly need a few limitations, *a priori* information with a specific aim to improve interpretable and reasonable model parameters [1]. However, in almost every case, the measured SP anomaly was interpreted without considering the analytical signals or total gradient derived from SP measurements.

The main objective of the present work is to interpret the analytic signal amplitude (ASA) or the total gradient (TG) of SP anomaly over different idealized or causative body, which satisfies the Laplace's condition. It is well known that the analytical signals derived from SP anomaly are correctly known as the TG [71–74]. The interpretation of ASA or TG derived from SP has been sparsely done in the present literature. It was only interpreted using ant colony optimization (ACO) [75]. In the current work, very fast simulated annealing (VFSA) was applied to decide the different model parameters associated with idealized subsurface bodies for ASA or TG from SP anomalies. The present inversion method has an advantage over other approaches for its pliability and its proficiency to converge toward global optima. The method has an ability to avoid from getting stuck in local minima and it has very high resolution, faster calculation as well as less memory without negotiating the resolution of the model parameters [2, 3, 35, 76–80]. Moreover, it does not need a priori information for the elucidation of SP anomalies.

In this study, inversion using VFSA algorithm was performed with the help of synthetic noise-free and noise-corrupted synthetic data using single and multiple structures and two field data from Sulleymonkoy anomaly, Ergani, Turkey, Senneterre area of Quebec, Canada. The results from the present method were compared with other well-established SP anomaly interpretations, such as ACO techniques. The present method used as a comprehensive method for quantitative elucidation of SP anomalies derived after various subsurface idealized geobodies.

## 2. Methodology

### 2.1. Forward modeling

Following Nabighian [71], the 2-D analytical signal amplitude (ASA) or the total gradient (TG) of SP anomaly is given as.

$$ASA(x) = (V_x^2 + V_y^2)^{1/2} \tag{1}$$

where $V_x$ and $V_y$ are the horizontal and vertical derivatives of the SP anomalies, respectively. The 2-D ASA of few of the idealized geobodies can be estimated following the general expression of SP anomaly $ASA\ (x)$ for idealized causative bodies (horizontal/vertical cylinder, sphere, inclined sheet, etc.) at any point on the surface of the earth (**Figure 1**) [70, 71, 74, 75], which is given by the equation:

$$ASA(x) = k \left[ \frac{1}{[(x-x_0)^2 + (z)^2]^q} \right] \tag{2}$$

where $k$ is the amplitude coefficient/factor related to the physical properties of the source, $z$ is the depth from the surface to the top of the body (sphere, cylinder, sheet, line of poles, point pole), $x_0$ (i = 1, …,N) is the horizontal position coordinate on the surface, and $q$ is the shape factor. The shape factors ($q$) for horizontal/vertical cylinder, sphere, inclined sheet, line of poles, and point poles are 1, 1.5, 1, 0.5, and 1, respectively. The total derivation of the ASA or TG anomaly can be found in various literatures [71–75, 81].

The above equation can be used to interpret single structure. However, in order to interpret the numerous structures, the expression (2) can be rewritten as [36]:

$$ASA(x_i) = \sum_{j=1}^{M} ASA_j(x_i) \tag{3}$$

where $ASA_j\ (x_i)$ is the SP anomaly at $x_i$ location for $j$th body and $M$ is the number of bodies.

### 2.2. Global optimization

Several global optimization approaches have been effectively used in interpretation of different geophysical data (e.g., [35–37, 75, 77, 82–86]). In the present study, an alternative method
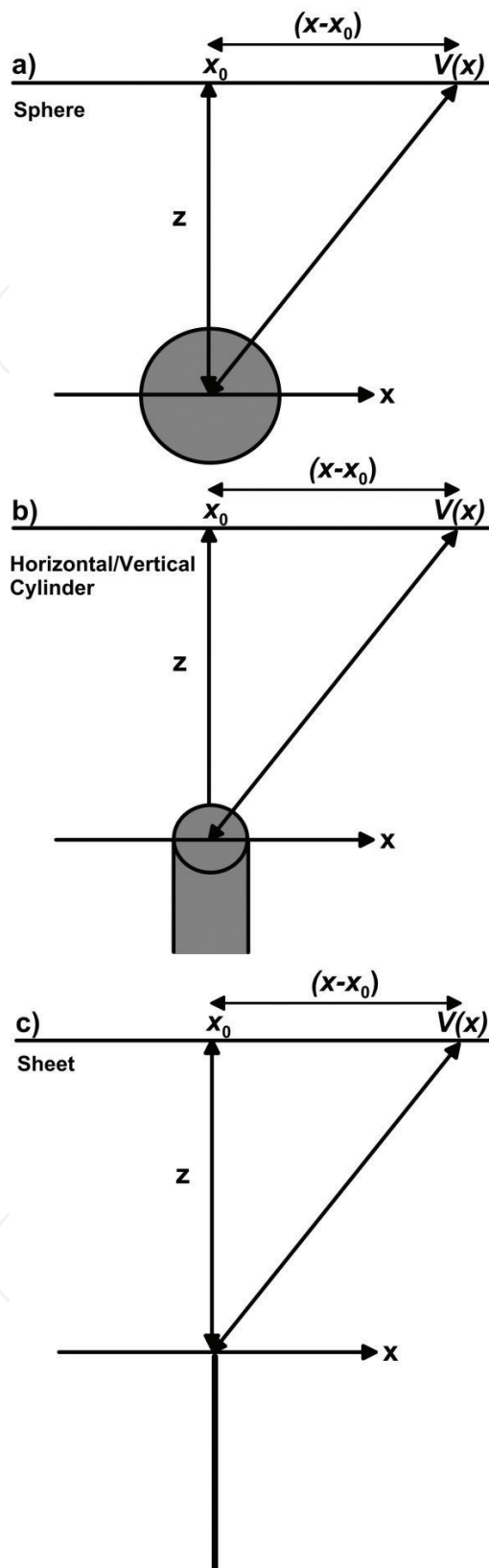
**Figure 1.** A diagram showing cross-sectional views, geometries, and parameters for (a) sphere, (b) cylinder, and (c) sheet-type structure.

of simulated annealing (SA) which is called as very fast simulated annealing (VFSA) was applied in the present study to elucidate the total gradient SP anomaly. VFSA is different from SA in terms of faster cooling schedule due to its finer Cauchy probability distribution for the arbitrary selection of every model parameter. VFSA takes any value in a model space, whereas SA does it in a predefined model space and hence the resolution increases for VFSA. Moreover, in VFSA optimization process, it does not recall all models and hence needs very small memory [35, 87, 88]. In every geophysical inversion, the main objective is to minimize the error function or the misfit. In the present work, the misfit ($\varphi$) between the observed and calculated/model response was used for SP data interpretation because of the fact that the objective function gets affected (increases) near zero crossing of SP anomaly (after [78]).

$$\phi = \frac{1}{N} \sum_{i=1}^{N} \left( \frac{v_i^0 - v_i^c}{|v_i^0| + (v_{max}^0 - v_{min}^0)/2} \right)^2 \tag{4}$$

where N is the number of data point, $v_i^0$ and $v_i^c$ are the $i$th observed and model responses and $v_{max}^0$ and $v_{min}^0$ are the maximum and minimum values of the observed response, respectively.

For the present inversion of SP data using VFSA optimization process, different parameters such as initial temperature, cooling schedule, number of iterations, and number of moves per temperature were taken as 1.0, 0.4, 2000, and 50. To find out the global/optimum solution, probability density function (PDF) was taken within 60.65% limit and ambiguity study has also been carried out based on the techniques developed by Mosegaard and Tarantola [89], Sen and Stoffa [90]. The details of the inversion process can be found in different literatures such as Sen and Stoffa [77], Sharma [86], Sharma and Biswas [78], Biswas [82], and Biswas [5]. Because in the earlier studies, the VFSA algorithm has established a very good performance as a powerful optimization method for estimating multidimensional and multimodal error functions. Hence, this optimization strategy is applied for SP data enhancement and regularization. The present VFSA algorithm for interpretation of ASA or TG of SP anomaly was carried out in Windows 8 environment using MS FORTRAN Developer studio on a simple desktop PC with Intel Core $i7$ processor. For each step of optimization, an overall of $10^6$ forward computations (2000 iteration × 50 number of moves × 10 VFSA runs) were accomplished and accepted models were stored in memory. The total time required (not CPU time) to compute a sole inversion is 35 s.

# 3. Results and discussion

## 3.1. Parameter search range

An appropriate selection of initial guess values or the search range for every model parameters is a significant objective of any inversion approach. For the quantitative elucidation of SP anomaly from ASA, the horizontal position of the source is found from the highest anomaly, the depth from half width [71], and the size of the amplitude from highest amplitude and depth. Srivastava and Agarwal [70] stated that the most stable parameter for interpretation of

SP anomaly is the horizontal location, which changes very little. Moreover, it was discussed earlier that limiting the shape factor also gives the consistent results in terms of ambiguity and error [35]. Hence, in order to find the accurate or the true value of each model parameter, initially the search ranges for each model parameters were kept wide so as to find out the most probable solution. Next, the search spaces were reduced to find the more appropriate results. When the model parameter gives the utmost results and very least error, the location ($x_0$) and the shape factor ($q$) were fixed to their real/true values to further reduce the error in the amplitude and the depth so as to find the actual depth of the subsurface bodies and reduce ambiguity in the final interpretation.

## 3.2. Synthetic examples

The VFSA inversion technique was utilized considering synthetic noise-free and noise-corrupted data (10 and 20% random noise) for self-potential anomaly for various subsurface structures derived from the ASA anomaly. At first, every model parameter was inverted for every data. Synthetic hypothetical data were produced utilizing Eq. (2) for different idealized geobodies, and 10 and 20% random noise is corrupted to the synthetic data. VFSA inversion was applied utilizing noise-free and noisy data to retrieve the genuine model parameters and analyze the impact of noise on the deciphered model parameters. In general, a reasonable search range/space for every model parameter was chosen and one VFSA run was performed. Thereafter, the best possible convergence of every model parameter was studied ($k$, $x_0$, $z$, and $q$) and misfit.

Next, to acquire the mean model, 10 VFSA runs were executed. At that point, histograms were constructed from the retrieved models whose misfit error was lesser than $10^{-4}$. Then, a statistical mean model was calculated utilizing models that have misfit lesser than $10^{-4}$, which also exist inside one standard deviation. Besides, cross-plots were also developed and analyzed to check whether the model parameters were inside the high PDF region (60.65%). Further, noises were also added in the data and the process was repeated again where the misfit error was lower than $10^{-2}$. Finally, the comparison between the observed and model responses was shown for every model. This process was applied for each hypothetical synthetic noise-free, noisy, and field cases.

### 3.2.1. Model 1 (sphere)

Inversion of the SP data was performed as said above utilizing synthetic noise-free data for sphere-like structure. **Figure 2** demonstrates the convergence example for every model parameter. **Figure 3a** demonstrates the histogram for every model parameter ($k$, $x_0$, and $z$). The histogram uncovers that all the parameters of the body can be very much interpretable after inversion. Moreover, very less ambiguity in the interpretation of the main three model parameters was found. The cross-plots analysis (**Figure 4a**) demonstrated that the model parameters were near their true value (green). The final estimated model parameters were within the ambiguity limits and inside the high PDF region (red). The fittings between the observed and model response are shown in **Figure 6a**. The deduced model parameters and mean model are shown in **Table 1**. Next, another model was also selected to see the variation in the amplitude, location, and depth. Inversion was repeated the same way as discussed above. **Figure 3b**
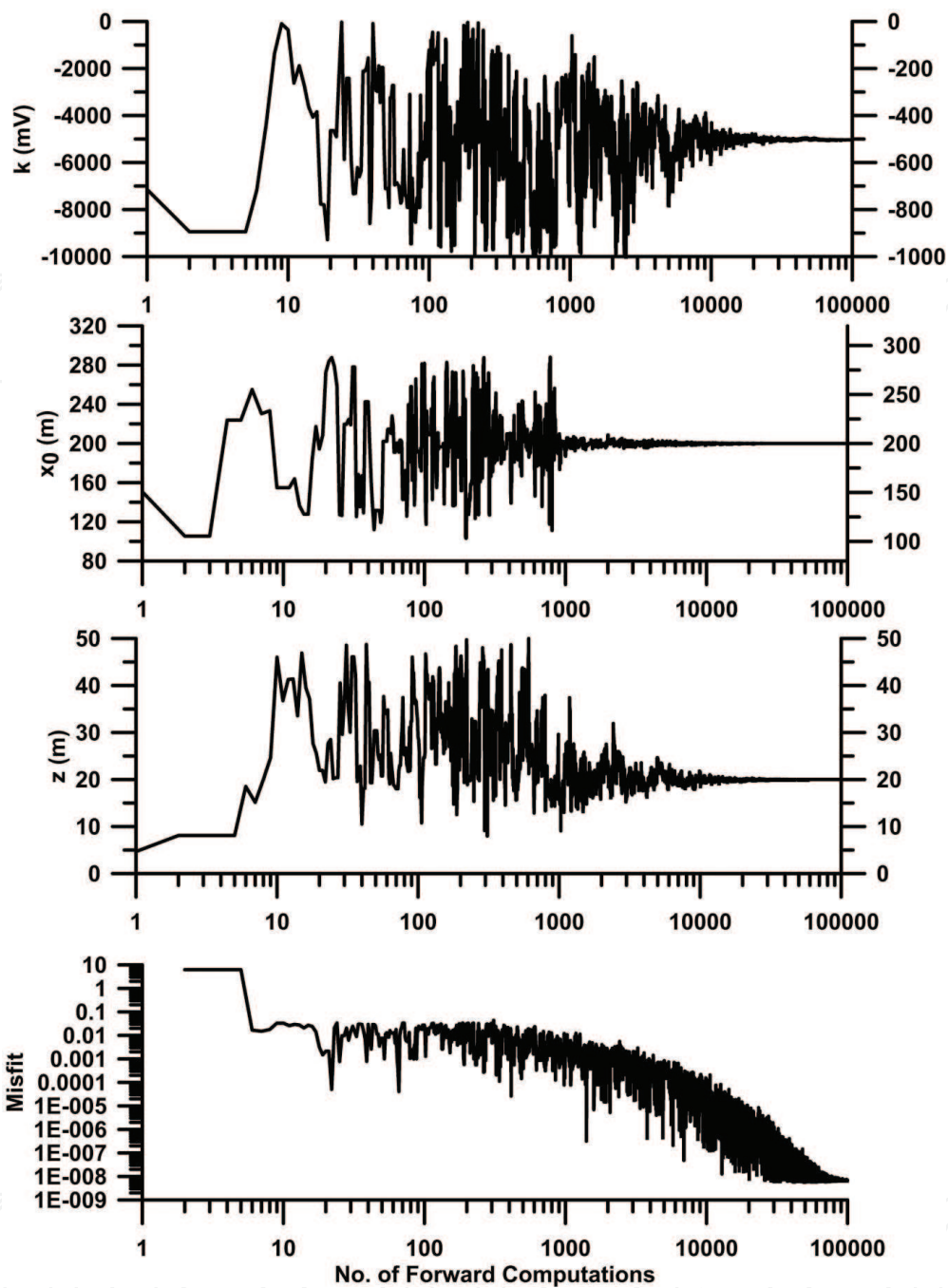
**Figure 2.** Convergence pattern for various model parameters and misfit.

shows the histogram for the three model parameters. **Figure 5a** demonstrates the cross-plots for this model as well. The fittings between the observed and model response are shown in **Figure 6b**, and the elucidated parameters and mean model are shown in **Table 2**.

### 3.2.2. Model 2 (horizontal and vertical cylinder)

Another synthetic example for horizontal and vertical cylinder-like body was taken for inversion of the SP data. **Figure 7a** shows the histogram for every model parameter ($k$, $x_0$, and $z$).
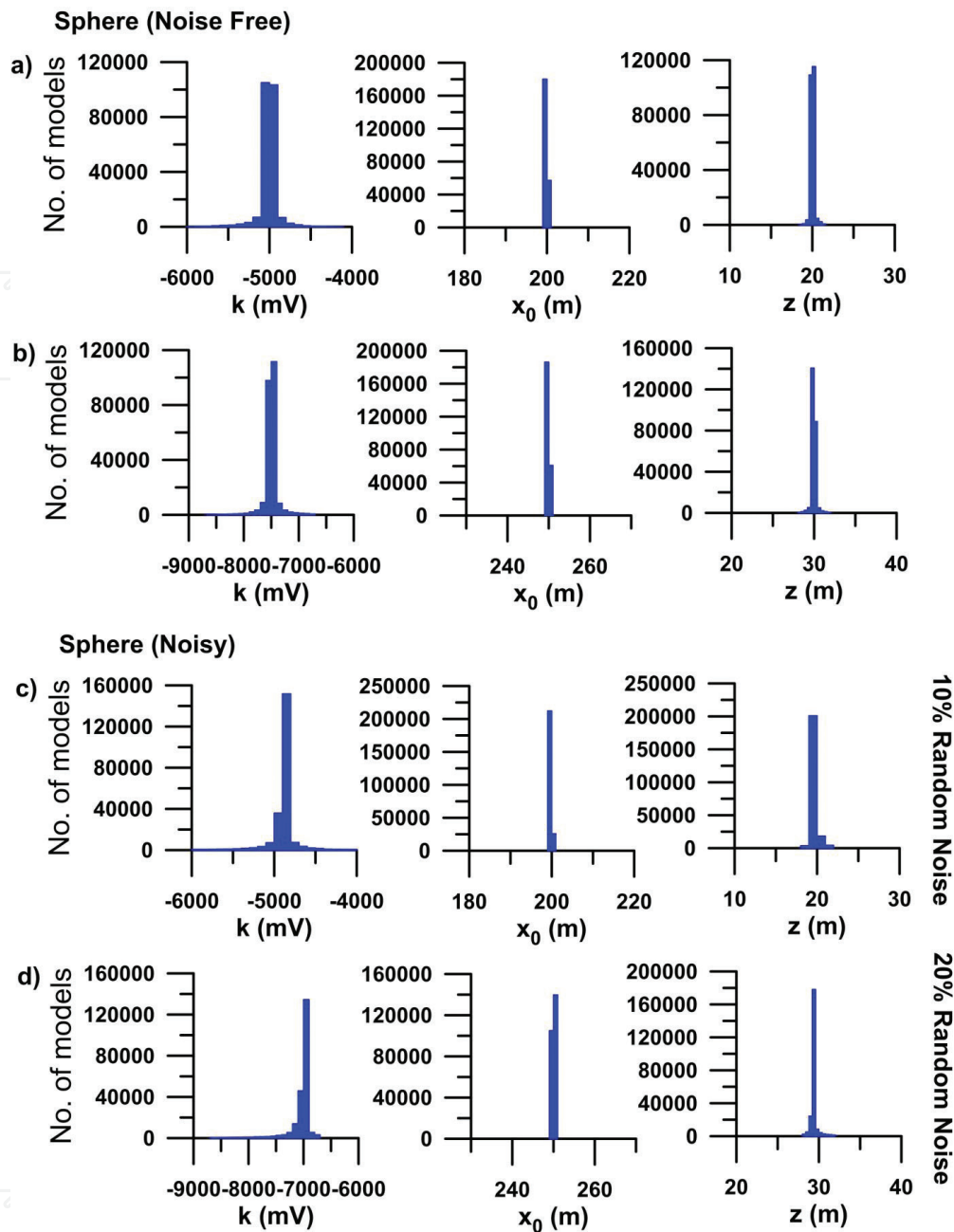
**Figure 3.** (a and b) Histograms of all accepted models having misfit <10−4 for noise-free synthetic data for sphere and (c and d) histograms of all accepted models having misfit <10−2 for noisy synthetic data (10 and 20% random noise) for sphere.

The histogram shows that all the parameters of the cylindrical structure can be very much elucidated. The cross-plots analysis (**Figure 8a**) demonstrates that the model parameters were near their true value (green) and the final expected model parameters were within the ambiguity limits and within high PDF region (red). Observed and model response fits are shown in **Figure 10a**. The elucidated parameters and mean model are shown in **Table 3**. Similarly, for the sphere-like structure, another model was selected to see the variation in the model parameters. **Figure 7b** demonstrates the histogram for the three model parameters. **Figure 9a**
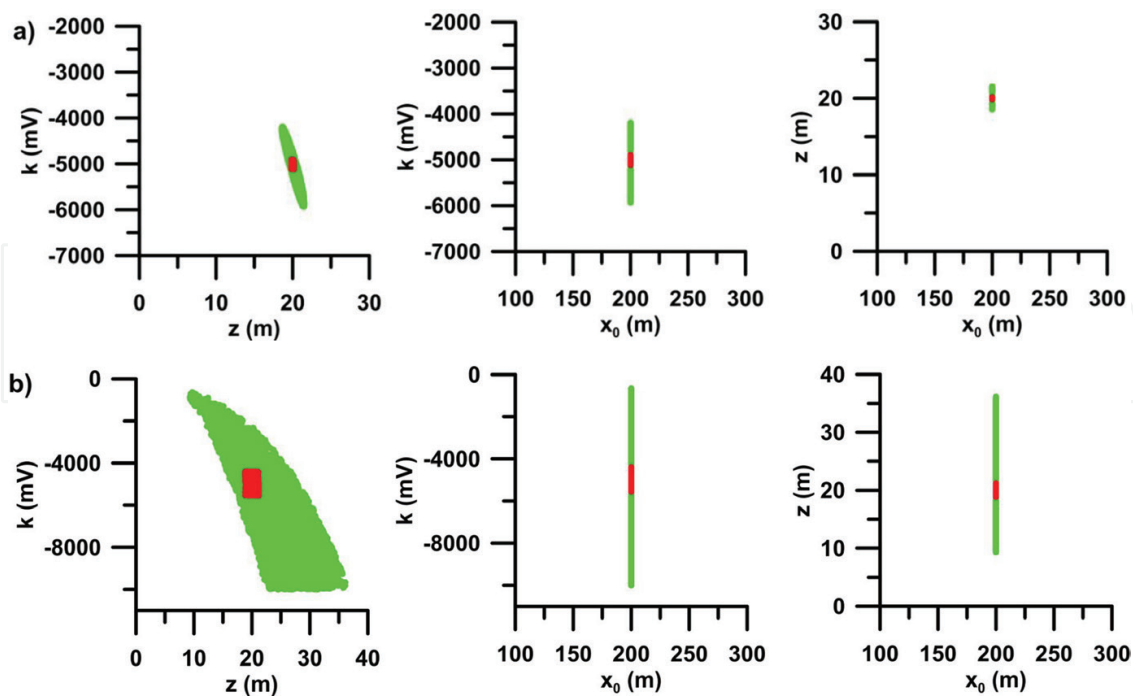
**Figure 4.** (a) Cross-plots between amplitude coefficient ($k$), depth ($z$), shape location ($x_0$) for all models having misfit < threshold ($10^{-4}$ for noise-free data) (green), and models with PDF > 60.65% (red) for noise-free data, (b) cross-plots between amplitude coefficient ($k$), depth ($z$), shape location ($x_0$) for all models having misfit < threshold ($10^{-2}$ for noisy data) (green), and models with PDF > 60.65% (red) for noisy (10% random) data for sphere.

| Model parameters | Actual value | Search range | Mean model (noise-free) | Mean model (noisy data) |
|---|---|---|---|---|
| $k$ (mV) | −5000 | −10,000 to 0 | −5002.2 ± 27.4 | −4907.7 ± 152.2 |
| $x_0$ (m) | 200 | 0–300 | 200.0 ± 0.0 | 200.0 ± 0.0 |
| $z$ (m) | 20 | 0–50 | 20.0 ± 0.0 | 19.9 ± 0.3 |
| $q$ | 1.5 | 0–2 | 1.5 ± 0.0 | 1.5 ± 0.0 |
| Misfit | | | $6.6 \times 10^{-9}$ | $9.4 \times 10^{-5}$ |

**Table 1.** Actual model parameters, search range, and interpreted mean model for noise-free, 10% random noise with uncertainty for sphere.

demonstrates the cross-plots of this model. Observed and model responses are shown in **Figure 10b**, and the elucidated parameters and mean model are shown in **Table 4**.

### 3.2.3. Model 3 (inclined sheet)

A synthetic example for 2-D inclined sheet-type body was also taken for inversion of the SP data. **Figure 11a** shows the histogram for every model parameter ($k$, $x_0$, and $z$). The cross-plots (**Figure 12a**) also demonstrate that the model parameters are near their actual value (green) and the final plausible model parameters lie inside the estimated ambiguity limits and inside high PDF region (red). Observed and model response fits are shown in **Figure 14a**. The elucidated
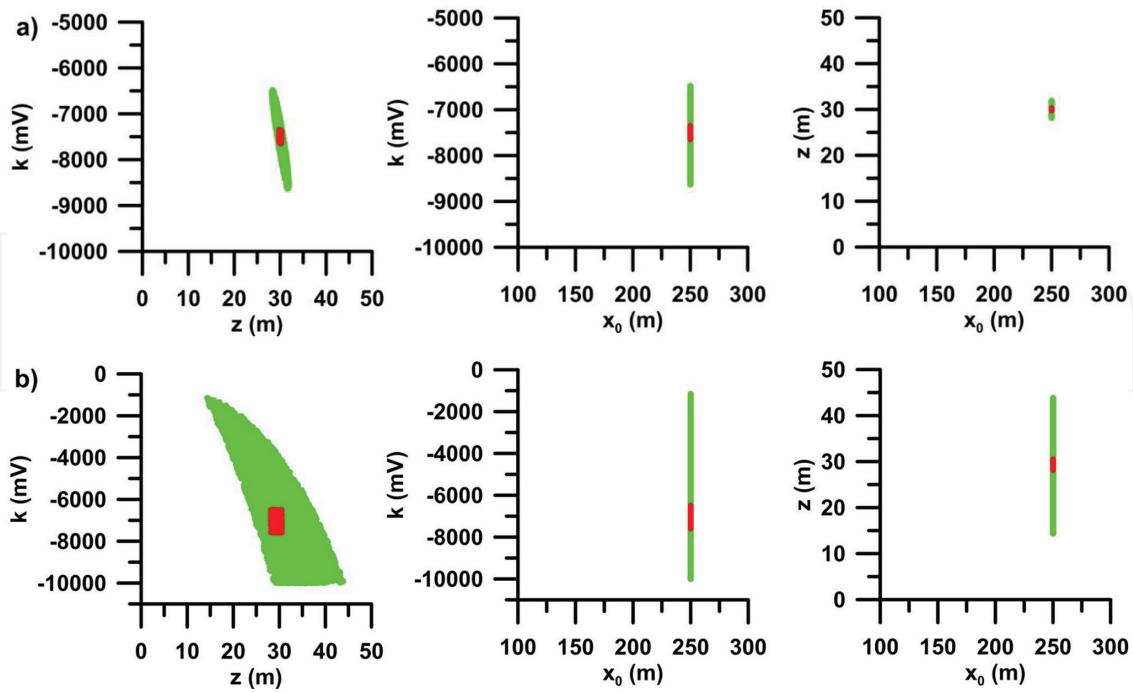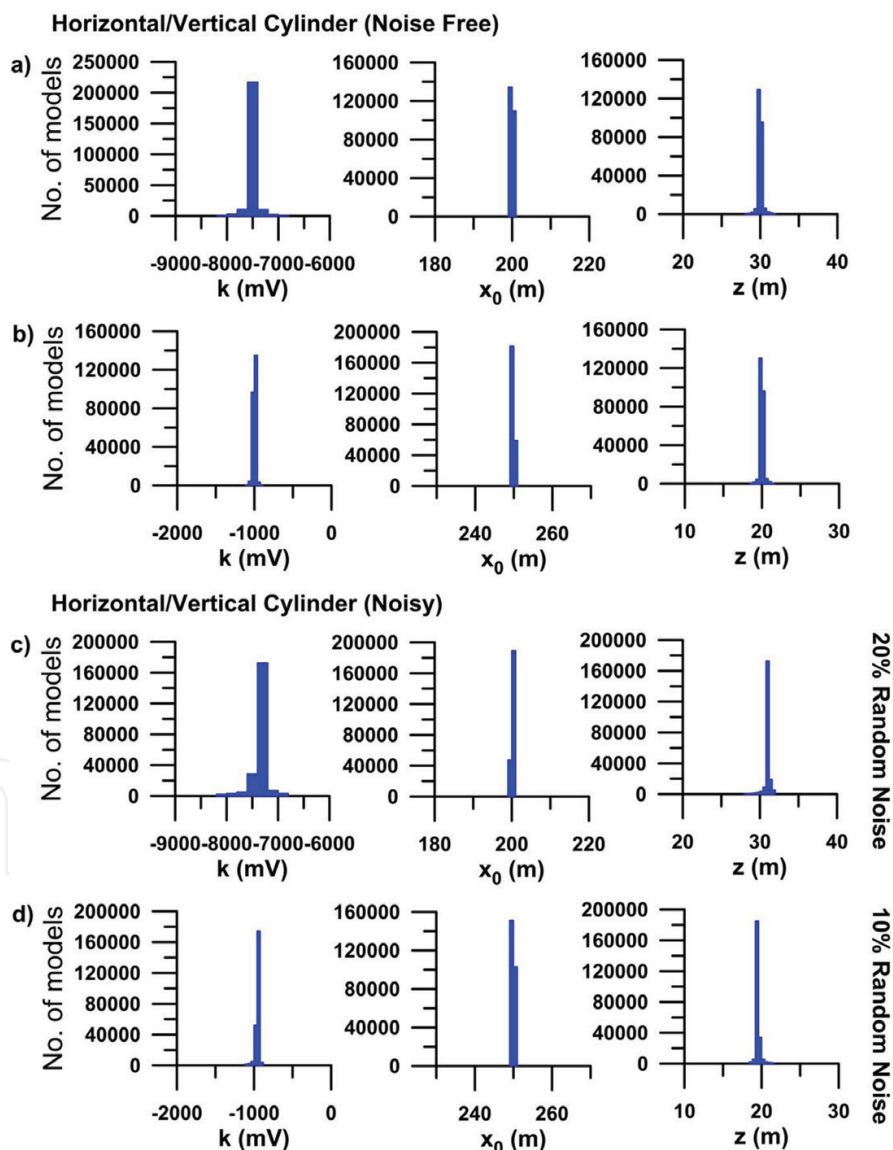
**Figure 5.** (a) Cross-plots between amplitude coefficient ($k$), depth ($z$), shape location ($x_0$) for all models having misfit < threshold ($10^{-4}$ for noise-free data) (green), and models with PDF > 60.65% (red) for noise-free data, (b) cross-plots between amplitude coefficient ($k$), depth ($z$), shape location ($x_0$) for all models having misfit < threshold ($10^{-2}$ for noisy data) (green), and models with PDF > 60.65% (red) for noisy (20% random) data for sphere.
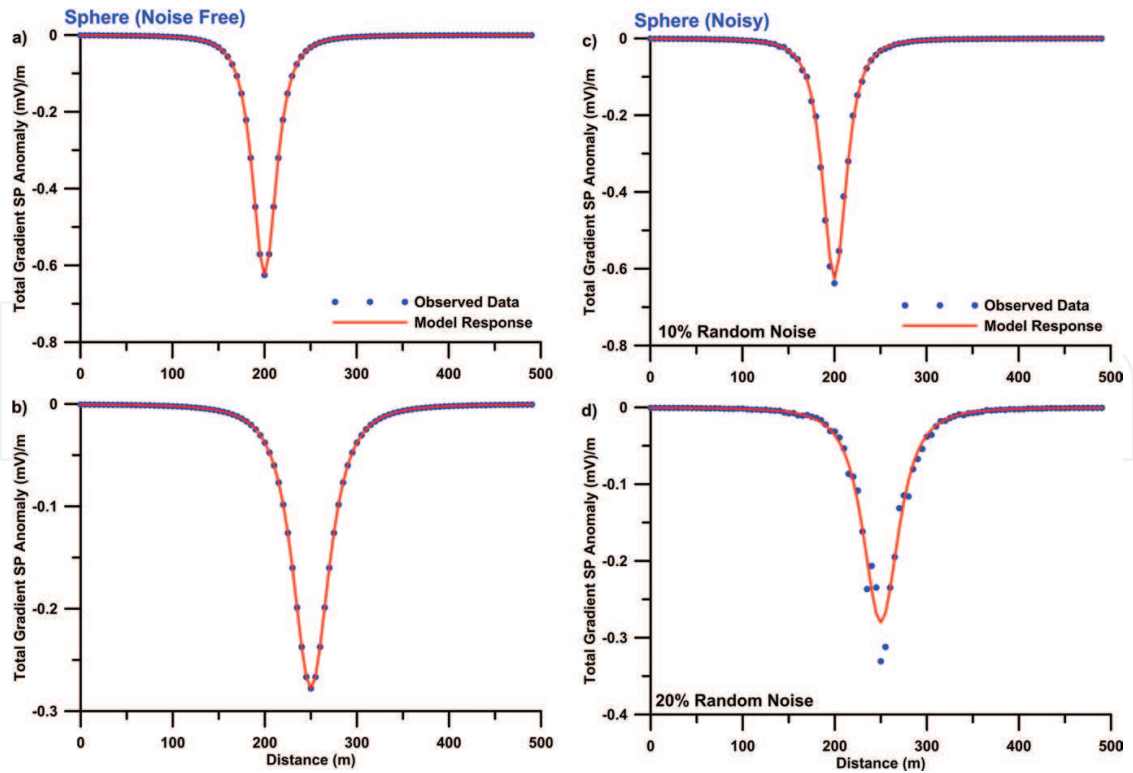


**Figure 6.** Fittings between the observed and model responses for sphere—(a) noise-free synthetic data; (b) noise-free synthetic data; (c) 10% random noisy synthetic data; and (d) 20% random noisy synthetic data.

| Model parameters | Actual value | Search range | Mean model (noise-free) | Mean model (noisy data) |
|---|---|---|---|---|
| $k$ (mV) | −7500 | −10,000 to 0 | −7497.4 ± 34.6 | −7037.4 ± 151.6 |
| $x_0$ (m) | 250 | 0–300 | 250.0 ± 0.0 | 250.0 ± 0.0 |
| $z$ (m) | 30 | 0–50 | 30.0 ± 0.0 | 29.9 ± 0.3 |
| $q$ | 1.5 | 0–2 | 1.5 ± 0.0 | 1.5 ± 0.0 |
| Misfit | | | $4.2 \times 10^{-8}$ | $7.1 \times 10^{-4}$ |

**Table 2.** Actual model parameters, search range, and interpreted mean model for noise-free, 20% random noise with uncertainty for sphere.



**Figure 7.** (a and b) Histograms of all accepted models having misfit < $10^{-4}$ for noise-free synthetic data for cylinder and (c and d) histograms of all accepted models having misfit < $10^{-2}$ for noisy synthetic data (20 and 10% random noise) for cylinder.
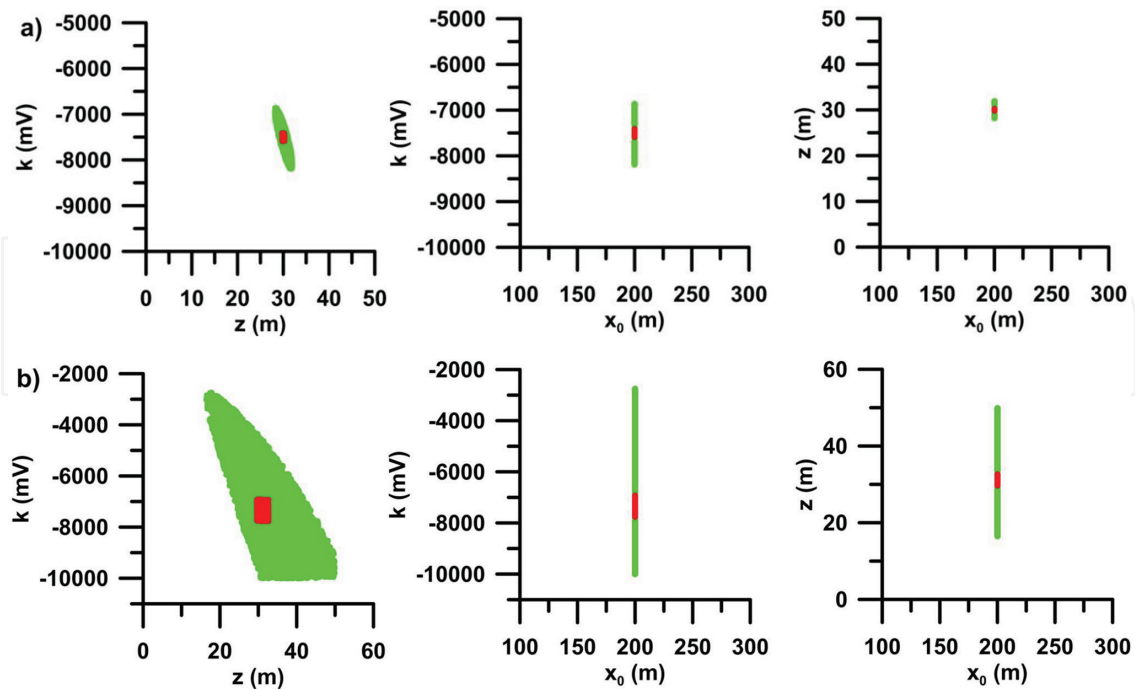
**Figure 8.** (a) Cross-plots between amplitude coefficient ($k$), depth ($z$), shape location ($x_0$) for all models having misfit < threshold ($10^{-4}$ for noise-free data) (green), and models with PDF > 60.65% (red) for noise-free data, (b) cross-plots between amplitude coefficient ($k$), depth ($z$), shape location ($x_0$) for all models having misfit < threshold ($10^{-2}$ for noisy data) (green), and models with PDF > 60.65% (red) for noisy (10% random) data for cylinder.

| Model parameters | Actual value | Search range | Mean model (noise-free) | Mean model (noisy data) |
|---|---|---|---|---|
| $k$ (mV) | −7500 | −10,000 to 0 | −7497.9 ± 23.7 | −7357.3 ± 122.8 |
| $x_0$ (m) | 200 | 0–300 | 200.0 ± 0.0 | 200.0 ± 0.0 |
| $z$ (m) | 30 | 0–50 | 30.0 ± 0.0 | 31.1 ± 0.4 |
| $q$ | 1.0 | 0–2 | 1.0 ± 0.0 | 1.0 ± 0.0 |
| Misfit | | | $5.2 \times 10^{-11}$ | $9.8 \times 10^{-4}$ |

**Table 3.** Actual model parameters, search range, and interpreted mean model for noise-free, 20% random noise with uncertainty for horizontal/vertical cylinder.

parameters and mean model are given in **Table 5**. Another model was selected to see the variation in the model parameters. **Figure 11b** displays the histogram for the three model parameters. **Figure 13a** shows the cross-plots of this model. Observed and model response fits are shown in **Figure 14b**, and the elucidated parameters and mean model are shown in **Table 6**.

### 3.3. Noise analysis

To see the effectiveness of the present inversion results, the synthetic noise-free data must be corrupted with different degrees of noises and reinterpreted using the inversion method to check its performance and robustness of the method. Hence, 10 and 20% random noise was added to the data for sphere, cylinder, and sheet-type structure, and the procedure was repeated again to examine the effect of noise. **Figure 3c** and **d** displays the histogram for noise-corrupted
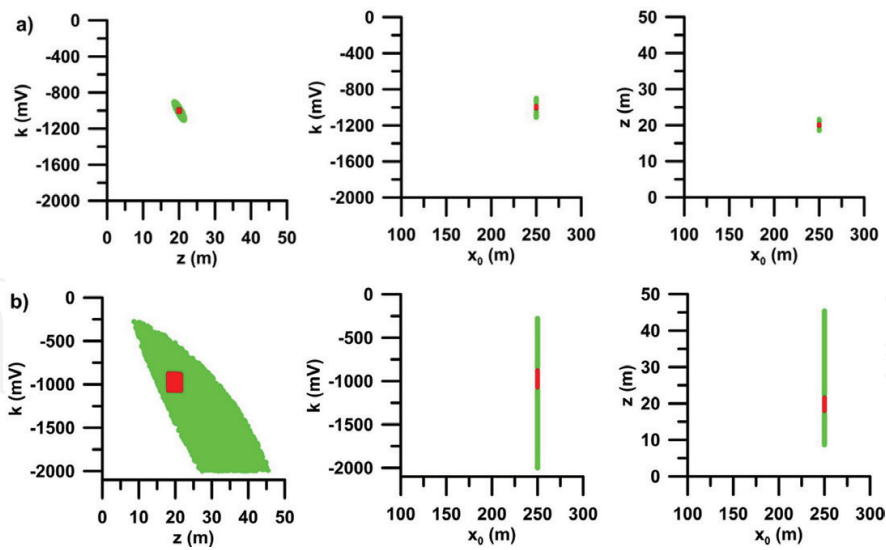
**Figure 9.** (a) Cross-plots between amplitude coefficient ($k$), depth ($z$), shape location ($x_0$) for all models having misfit < threshold ($10^{-4}$ for noise-free data) (green), and models with PDF > 60.65% (red) for noise-free data, (b) cross-plots between amplitude coefficient ($k$), depth ($z$), shape location ($x_0$) for all models having misfit < threshold ($10^{-2}$ for noisy data) (green), and models with PDF > 60.65% (red) for noisy (20% random) data for cylinder.
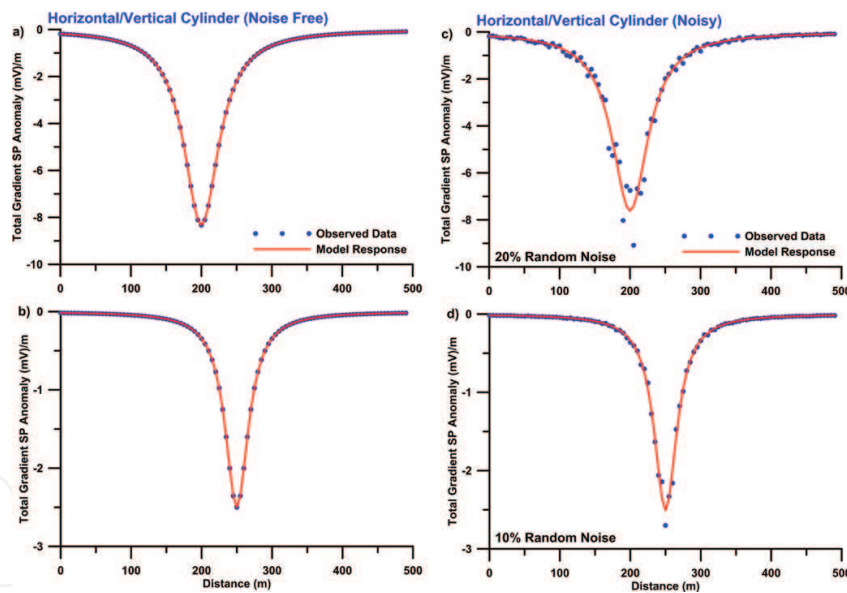


**Figure 10.** Fittings between the observed and model responses for cylinder—(a) noise-free synthetic data; (b) noise-free synthetic data; (c) 10% random noisy synthetic data; and (d) 20% random noisy synthetic data.

sphere-like structure. **Figures 4b** and **5b** show the cross-plots for noisy data. **Tables 1** and **2** show the interpreted mean model for noisy data and the fits between the observed and model response for noisy model are shown in **Figure 6c** and **d**. For horizontal and vertical cylinder-like structure, again noise was corrupted with the two models mentioned above. **Figure 7c** and **d** shows the histogram for noise-corrupted horizontal/vertical-like structure. **Figures 8b** and **9b** show the cross-plots for noisy data. **Tables 3** and **4** show the interpreted mean model for noisy data and the fits between the observed and model response for noisy model are shown in **Figure 10c** and **d**. Also, for 2-D inclined sheet-type structure, the same amount of noise was

| Model parameters | Actual value | Search range | Mean model (noise-free) | Mean model (noisy data) |
|---|---|---|---|---|
| $k$ (mV) | −1000 | −2000 to 0 | −999.6 ± 3.3 | −963.1 ± 22.6 |
| $x_0$ (m) | 250 | 0–300 | 250.0 ± 0.0 | 250.0 ± 0.0 |
| $z$ (m) | 20 | 0–50 | 20.0 ± 0.0 | 19.6 ± 0.4 |
| $q$ | 1.0 | 0–2 | 1.0 ± 0.0 | 1.0 ± 0.0 |
| Misfit | | | $5.9 \times 10^{-9}$ | $1.6 \times 10^{-4}$ |

**Table 4.** Actual model parameters, search range, and interpreted mean model for noise-free, 10% random noise with uncertainty for horizontal/vertical cylinder.
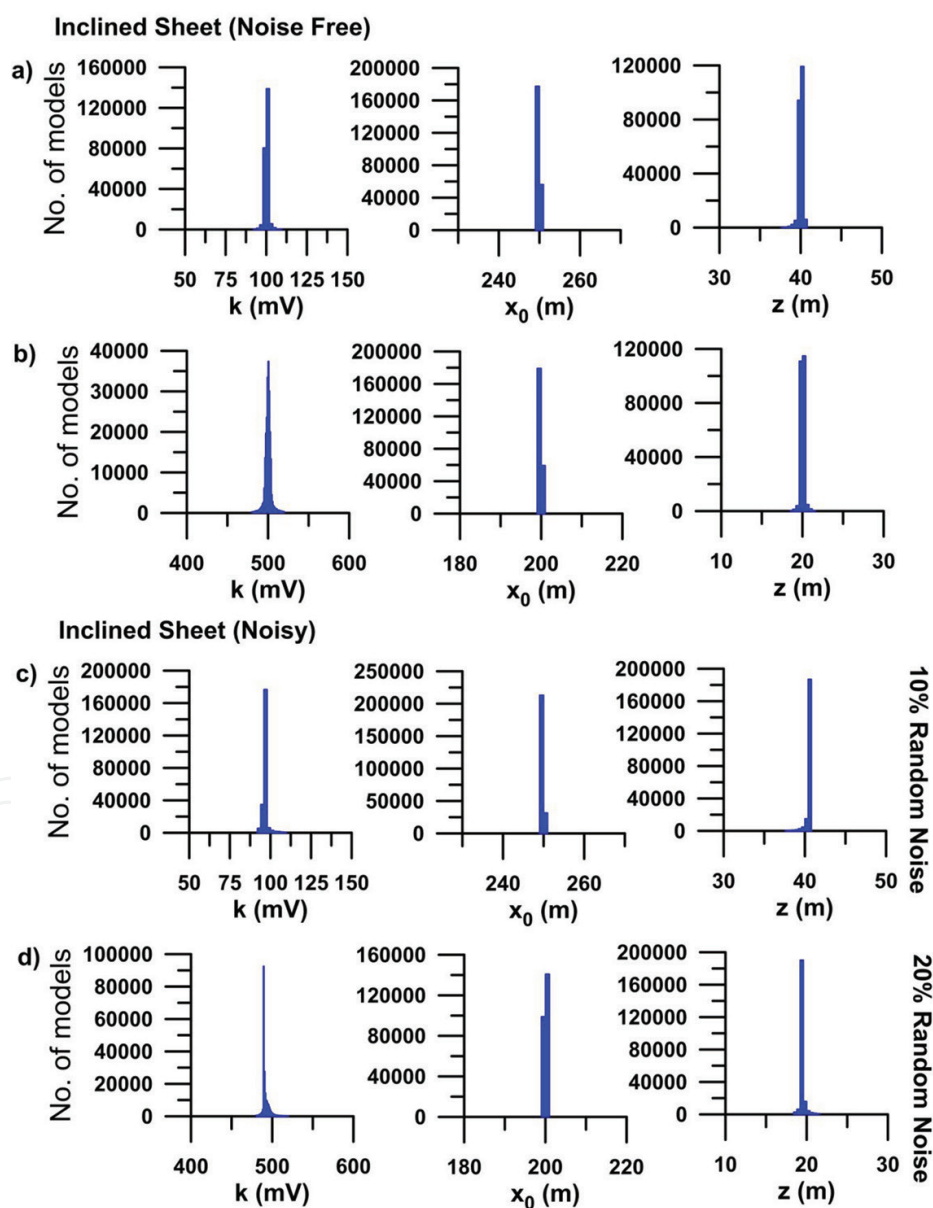


**Figure 11.** (a and b) Histograms of all accepted models having misfit < 10⁻⁴ for noise-free synthetic data for cylinder and (c, d) histograms of all accepted models having misfit < 10⁻² for noisy synthetic data (10 and 20% random noise) for sheet.
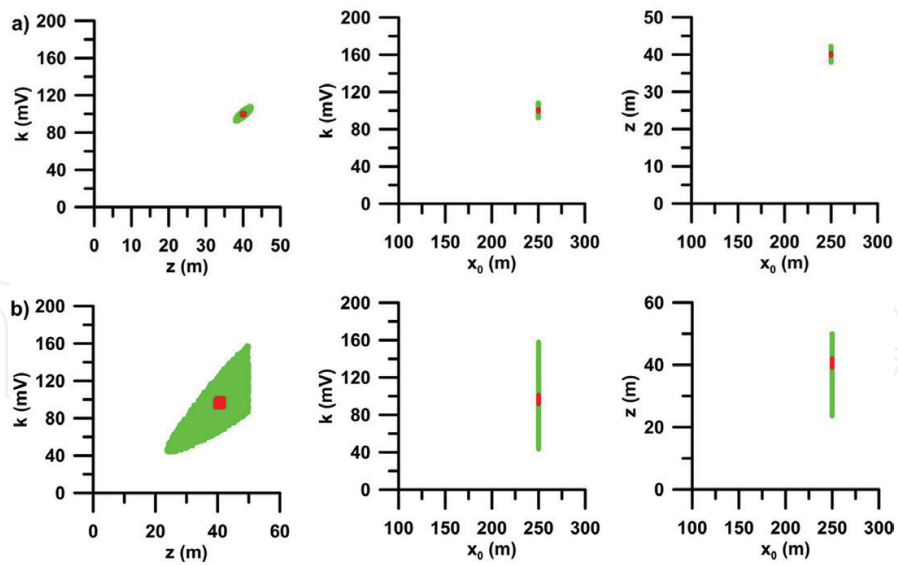
**Figure 12.** (a) Cross-plots between amplitude coefficient ($k$), depth ($z$), shape location ($x_0$) for all models having misfit < threshold ($10^{-4}$ for noise-free data) (green), and models with PDF > 60.65% (red) for noise-free data, (b) cross-plots between amplitude coefficient ($k$), depth ($z$), shape location ($x_0$) for all models having misfit < threshold ($10^{-2}$ for noisy data) (green), and models with PDF > 60.65% (red) for noisy (10% random) data for sheet.

| Model parameters | Actual value | Search range | Mean model (noise-free) | Mean model (noisy data) |
|---|---|---|---|---|
| $k$ (mV) | 100 | 0–200 | 100.1 ± 0.4 | 96.3 ± 1.2 |
| $x_0$ (m) | 250 | 0–300 | 250.0 ± 0.0 | 250.0 ± 0.0 |
| $z$ (m) | 40 | 0–50 | 40.0 ± 0.0 | 40.6 ± 0.4 |
| $q$ | 1.0 | 0–2 | 1.0 ± 0.0 | 1.0 ± 0.0 |
| Misfit | | | $4.7 \times 10^{-7}$ | $8.1 \times 10^{-5}$ |

**Table 5.** Actual model parameters, search range, and interpreted mean model for noise-free, 10% random noise with uncertainty for sheet.

corrupted in the models mentioned above. **Figure 11c** and **d** shows the histogram for noise-corrupted inclined sheet-type structure. **Figures 12b** and **13b** illustrate the cross-plots for noisy data. **Tables 5** and **6** show the interpreted mean model for noisy data and the fits between the observed and model response for noisy model are shown in **Figure 14c** and **d**. It can be seen from the study of histogram and cross-plots that the model parameters are interpreted very precisely, and it also advocates that the appraised model parameters for all structures are inside the ambiguity limits and within high PDF region. This also suggests that the inversion methodology developed for the elucidation of SP anomalies can precisely decide every model parameter and even if the data are highly corrupted with different degrees of noises.

## 3.4. Effect of complicated structure

It is significant to mention that that, in nature (field examples), it is very difficult to get an idealized geobody or structure. Moreover, the structures are mostly corrupted with different
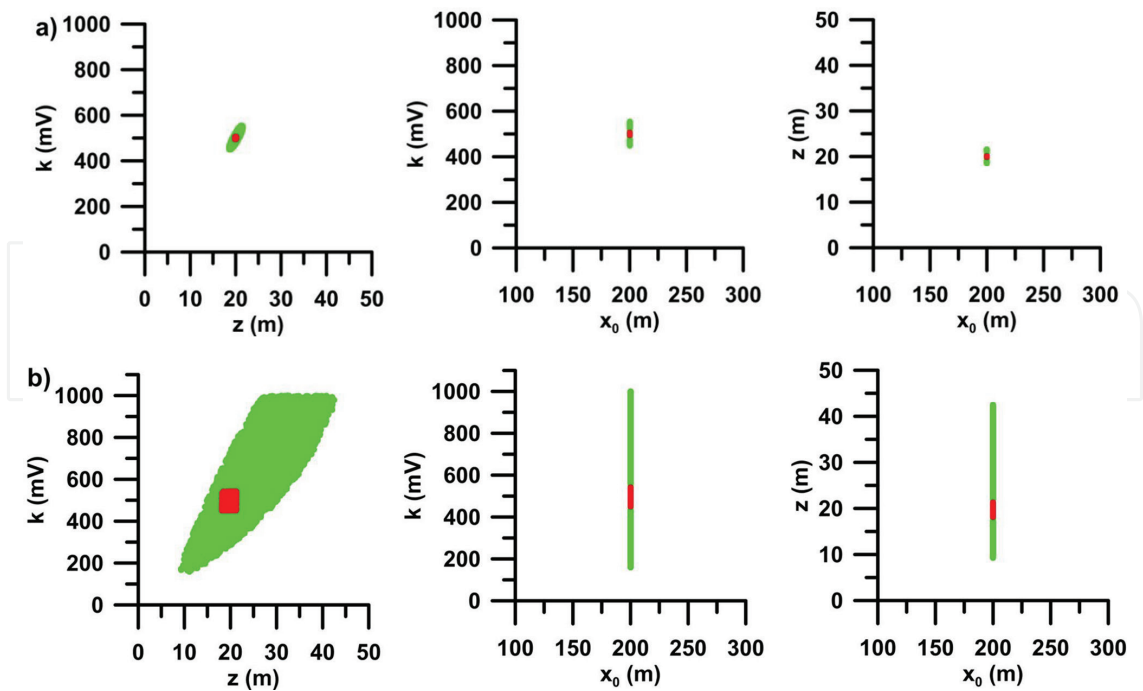
**Figure 13.** (a) Cross-plots between amplitude coefficient ($k$), depth ($z$), shape location ($x_0$) for all models having misfit < threshold ($10^{-4}$ for noise-free data) (green), and models with PDF > 60.65% (red) for noise-free data, (b) cross-plots between amplitude coefficient ($k$), depth ($z$), shape location ($x_0$) for all models having misfit < threshold ($10^{-2}$ for noisy data) (green), and models with PDF > 60.65% (red) for noisy (20% random) data for sheet.
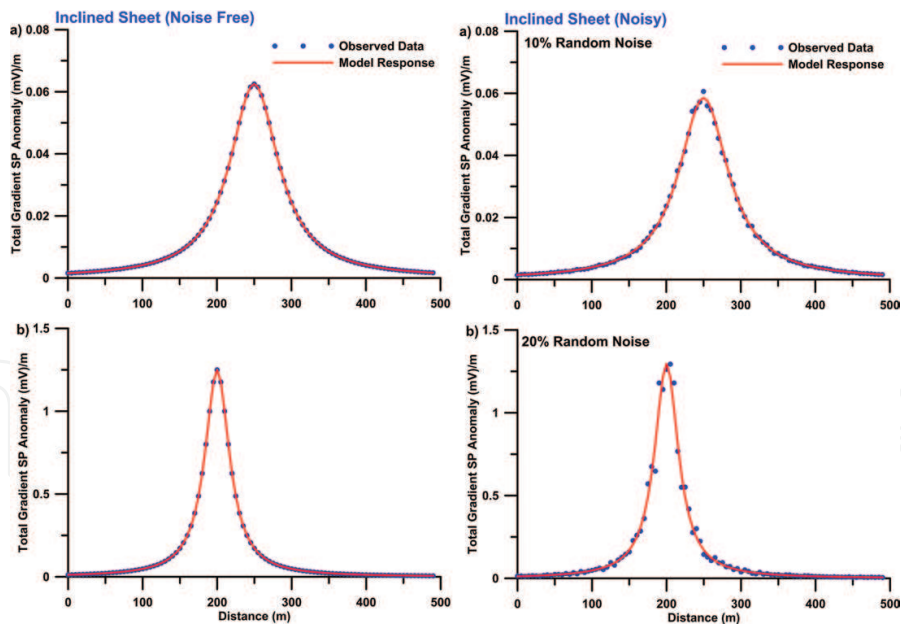


**Figure 14.** Fittings between the observed and model responses for sheet—(a) noise-free synthetic data; (b) noise-free synthetic data; (c) 10% random noisy synthetic data; and (d) 20% random noisy synthetic data.

degree of noises. Also, there might be multiple structures within the subsurface of different types. In those cases, the anomaly from multiple structures will be very difficult to interpret. To test whether the inversion method can accurately identify the multiple structures, three different structures were taken and forward responses have been computed using Eqs. (2)

| Model parameters | Actual value | Search range | Mean model (noise-free) | Mean model (noisy data) |
|---|---|---|---|---|
| $k$ (mV) | 500 | 0–1000 | $500.0 \pm 1.6$ | $493.5 \pm 10.5$ |
| $x_0$ (m) | 200 | 0–300 | $200.0 \pm 0.0$ | $200.0 \pm 0.0$ |
| $z$ (m) | 20 | 0–50 | $20.0 \pm 0.0$ | $19.5 \pm 0.3$ |
| $q$ | 1.0 | 0–2 | $1.0 \pm 0.0$ | $1.0 \pm 0.0$ |
| Misfit | | | $2.0 \times 10^{-9}$ | $6.2 \times 10^{-4}$ |

**Table 6.** Actual model parameters, search range, and interpreted mean model for noise-free, 20% random noise with uncertainty for sheet.
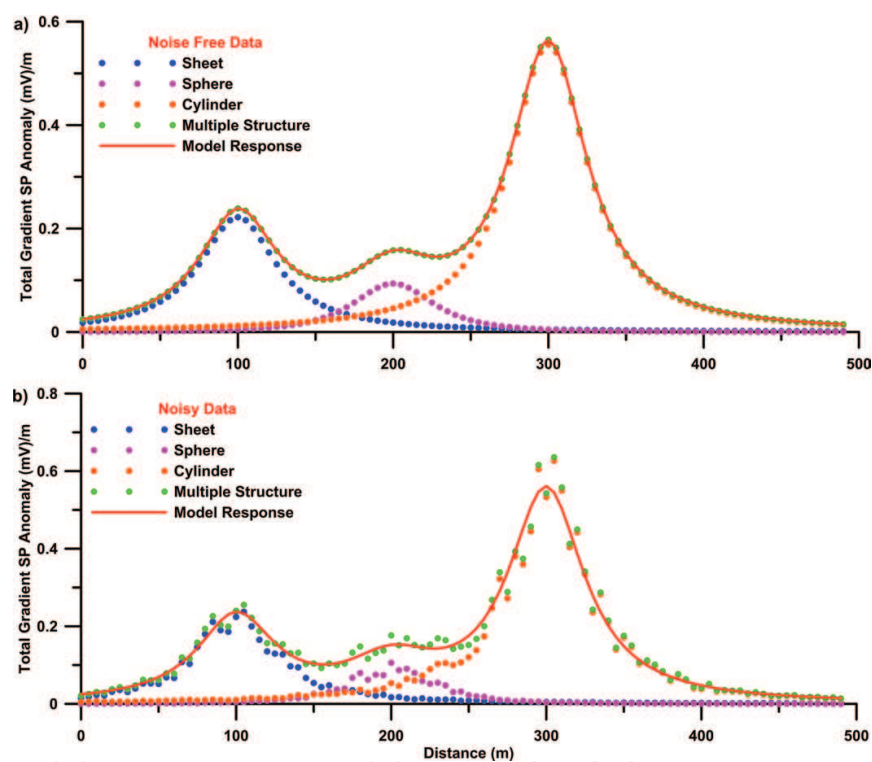


**Figure 15.** Fittings between the observed and model responses for multiple structure—(a) noise-free synthetic data; (b) 20% random noisy synthetic data.

and (3). Single structure and multiple structures from the forward modeling are shown in **Figure 15a**. Inversion of the synthetic data was carried out the same way as for the single model examples. Fits between the observed and model response are also shown in **Figure 15a**. Moreover, to investigate the effect of noisy data, only 20% random noise was corrupted in the data and inversion was repeated. **Figure 15b** displays the fits between the observed and model response for noisy data. **Table 7** shows the interpreted model parameters for each structure derived from the multiple anomalies. Both noise-free and noisy data are shown in **Table 7**. It can be seen from **Table 7** that the misfit is quite less for noise-free and noise-corrupted data. Histogram and cross-plots show alike as revealed in other examples for single structures. However, it is not presented here for brevity.

| Model parameters | Actual value | Search range | Sheet | Actual value | Search range | Sphere | Actual value | Search range | H/V cylinder |
|---|---|---|---|---|---|---|---|---|---|
| *Multiple bodies—noise-free* | | | | | | | | | |
| $k$ (mV) | 200 | 0–500 | $200.2 \pm 0.6$ | 6000 | 1000–10,000 | $6003.5 \pm 26.2$ | 500 | 100–1000 | $500.3 \pm 1.6$ |
| $x_0$ (m) | 100 | 0–200 | $100.0 \pm 0.0$ | 200 | 0–300 | $200.0 \pm 0.0$ | 300 | 50–200 | $300.0 \pm 0.0$ |
| $z$ (m) | 30 | 0–50 | $30.0 \pm 0.1$ | 40 | 0–50 | $40.0 \pm 0.0$ | 30 | 0–100 | $30.0 \pm 0.1$ |
| $q$ | 1.0 | 0–2 | $1.0 \pm 0.0$ | 1.5 | 0–2 | $1.5 \pm 0.0$ | 1.0 | 0–2 | $1.0 \pm 0.0$ |
| Misfit | | | $7.4 \times 10^{-8}$ | | | $3.3 \times 10^{-7}$ | | | $1.6 \times 10^{-8}$ |
| *Multiple bodies—20% random noise* | | | | | | | | | |
| $k$ (mV) | 200 | 0–500 | $205.4 \pm 4.3$ | 6000 | 1000–10,000 | $6316.9 \pm 133.6$ | 500 | 100–1000 | $485.4 \pm 11.0$ |
| $x_0$ (m) | 100 | 0–200 | $100.0 \pm 0.0$ | 200 | 0–300 | $200.0 \pm 0.0$ | 300 | 50–200 | $300.0 \pm 0.0$ |
| $z$ (m) | 30 | 0–50 | $30.5 \pm 0.5$ | 40 | 0–50 | $41.4 \pm 0.4$ | 30 | 0–100 | $29.7 \pm 0.5$ |
| $q$ | 1.0 | 0–2 | $1.0 \pm 0.0$ | 1.5 | 0–2 | $1.5 \pm 0.0$ | 1.0 | 0–2 | $1.0 \pm 0.0$ |
| Misfit | | | $7.8 \times 10^{-4}$ | | | $9.9 \times 10^{-4}$ | | | $1.2 \times 10^{-3}$ |

**Table 7.** Actual model parameters, search range, and interpreted mean model for noise-free and 20% random noise with uncertainty for multiple structure.

## 3.5. Field example

To demonstrate the efficiency of the present method, two field examples from Turkey and Canada were taken for interpretation. The field anomaly of ASA/TG from SP anomaly was taken from the earlier published literatures as described below:

### 3.5.1. Sulleymonkoy anomaly, Ergani, Turkey

This field example was taken from the Sulleymonkoy SP anomaly, Ergani, Turkey [91]. The ASA or TG anomaly was derived following Srivastava and Agarwal [70] (**Figure 18**). The anomaly was interpreted by many workers using different interpretation methods [38, 92–96]. The SP anomaly data were interpreted using the VFSA global optimization technique in this study. The TG anomaly shows a large magnitude peak anomaly with two small anomalies. In the present case, initially the main peak anomaly was interpreted considering a single structure. The depth obtained by the present study for single body was found to be 34.5 m on the horizontal location of 66.3 m, and the structure was interpreted as a cylindrical body. Histogram plot for single body (**Figure 16a**) also shows that the model parameters were precisely determined. Analysis of cross-plots (**Figure 17a**) also shows that the assessed model parameters were within the ambiguity limits. Next, considering multiple structures, the inversion process was repeated again for three different structures considering three peak values. Analysis of histogram plot for multiple bodies (**Figure 16b–d**) also shows that the model parameters were precisely determined. Investigation of cross-plots (**Figure 17b–d**) also shows that the estimated model parameters were within the uncertainty limits and
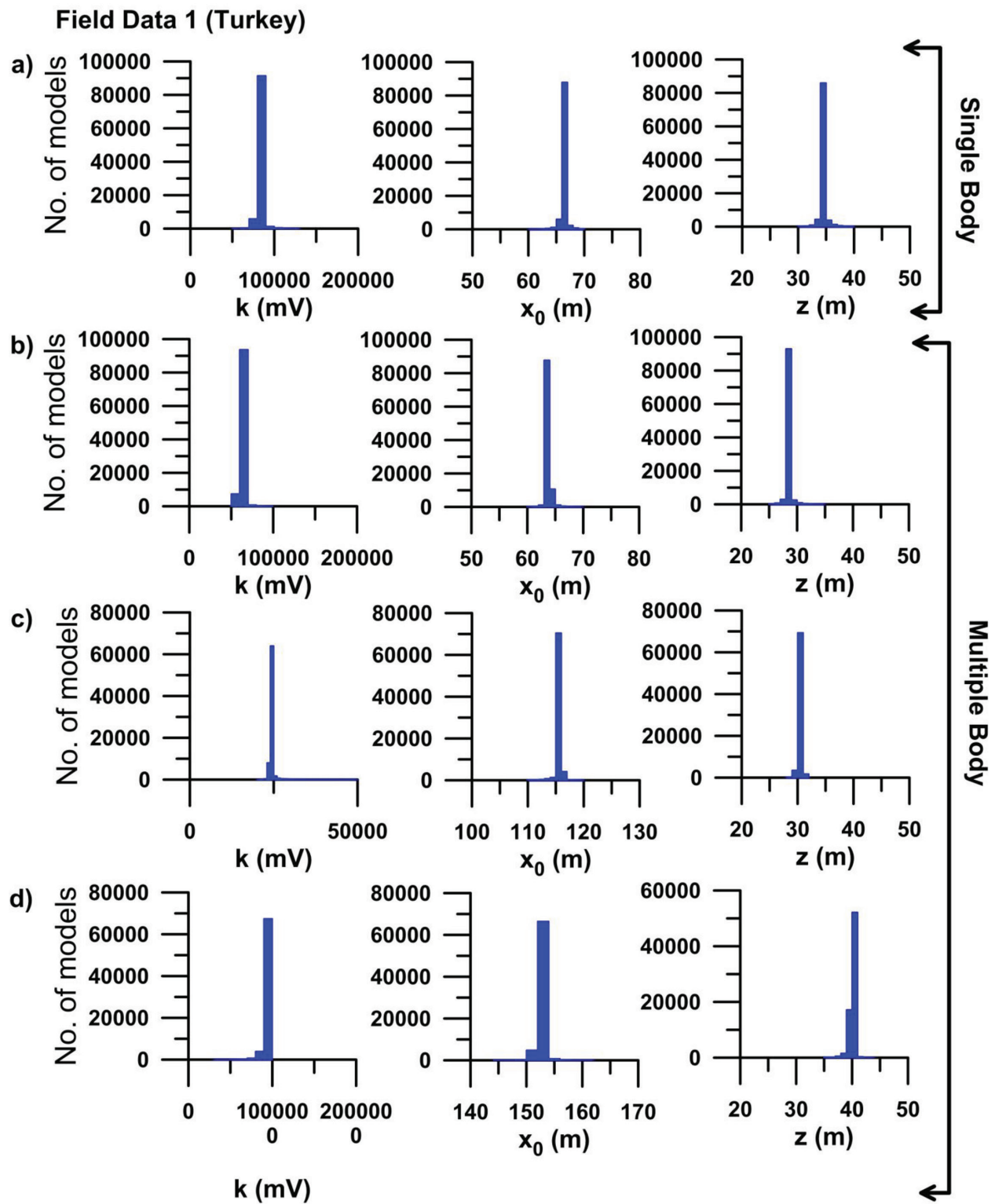
**Figure 16.** (a) Histograms of all accepted models having misfit < $10^{-2}$ for field data—single body and (b–d) histograms of all accepted models having misfit < $10^{-2}$ for field data—multiple bodies—Sulleymonkoy anomaly, Ergani, Turkey.

more precise than considering single body using the whole TG anomaly. However, the depth obtained for the peak anomaly was found to be 28.5 m on the location of 63.9 m considering multiple structures. The depth obtained by other workers such as Yungul [91] as 38.8 m, Bhattacharya and Roy [94] as 40.0 m, Agarwal [92] as 30.1 m, Sundararajan and Srinivas [96]
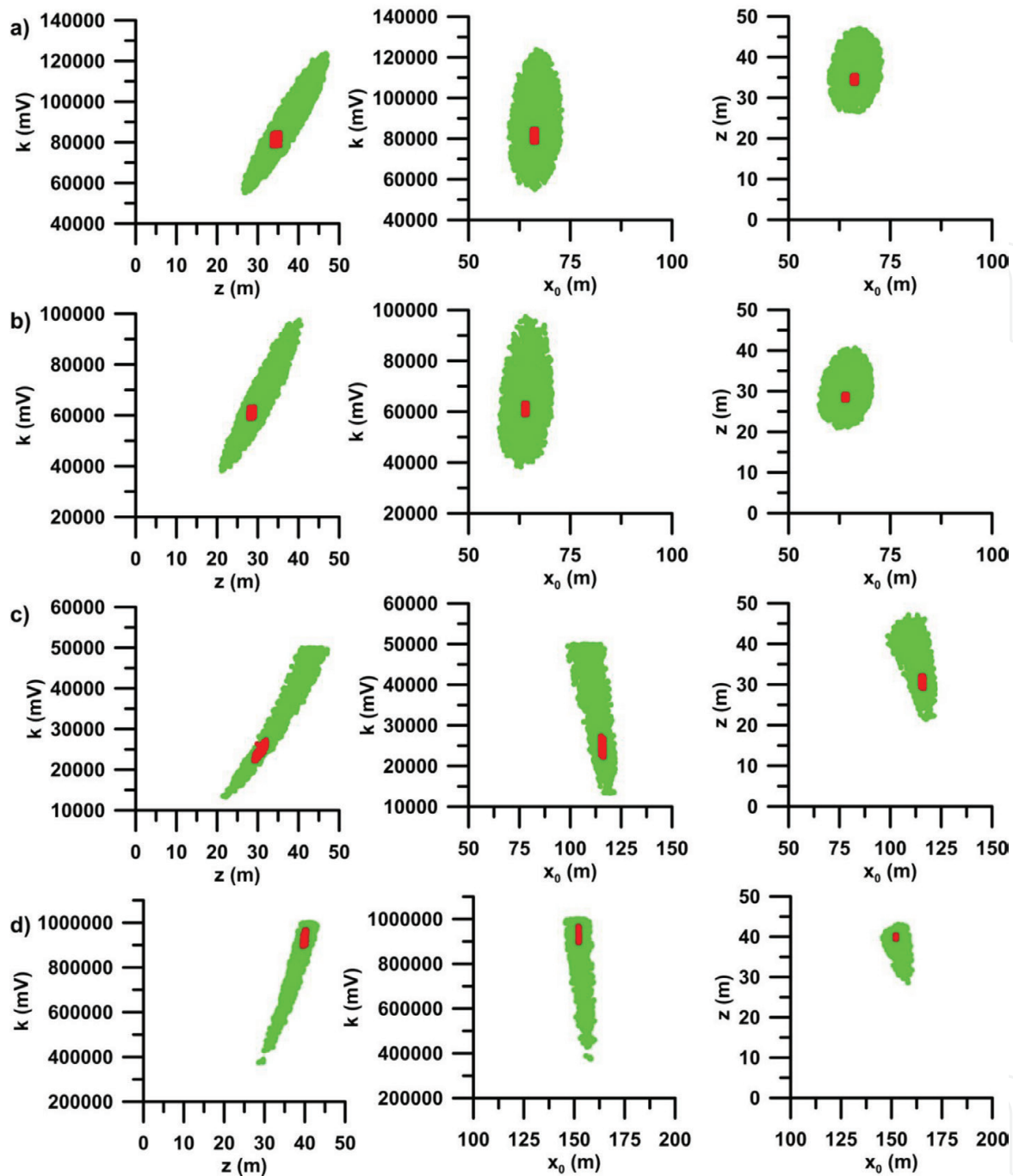
**Figure 17.** (a) Cross-plots between amplitude coefficient ($k$), depth ($z$), shape location ($x_0$) for all models having misfit < threshold ($10^{-2}$ for noise-free data) (green), and models with PDF > 60.65% (red) for field data—single body, (b–d) cross-plots between amplitude coefficient ($k$), depth ($z$), shape location ($x_0$) for all models having misfit < threshold ($10^{-2}$ for noise-free data) (green), and models with PDF > 60.65% (red) for field data—multiple bodies—Sulleymonkoy anomaly, Ergani, Turkey.

as 36 m, and Srivastava and Agarwal [95] as 28.9 m. Moreover, the estimated uncertainty was less considering multiple structures rather than a single body. **Table 8** shows a comparison between the different model parameters and misfit. **Figure 18** shows the comparison between the observed TG anomaly and the model response.

| Model parameters | Single body | | Multiple bodies | | | | | |
|---|---|---|---|---|---|---|---|---|
| | Search range | Present method B1 | Search range | Present method B1 | Search range | Present method B2 | Search range | Present method B3 |
| $k$ (mV) | 1000–200,000 | 81281.0 ± 957.5 | 1000–100,000 | 60888.2 ± 574.0 | 100–50,000 | 24244.9 ± 442.6 | 1000–1,000,000 | 935524.0 ± 12801.3 |
| $x_0$ (m) | 50–100 | 66.3 ± 0.2 | 50–100 | 63.9 ± 0.2 | 50–200 | 115.8 ± 0.2 | 50–200 | 152.3 ± 0.2 |
| $z$ (m) | 0–50 | 34.5 ± 0.3 | 0–50 | 28.5 ± 0.2 | 0–50 | 30.3 ± 0.3 | 0–100 | 40.0 ± 0.2 |
| $q$ | 0–2 | 1.0 | 0–2 | 1.0 | 0–2 | 1.0 | 0–2 | 1.0 |
| Misfit | | $5.6 \times 10^{-3}$ | | $9.8 \times 10^{-4}$ | | $8.5 \times 10^{-5}$ | | $1.4 \times 10^{-3}$ |

**Table 8.** Search range and interpreted mean model for Sulleymonkoy anomaly, Ergani, Turkey.
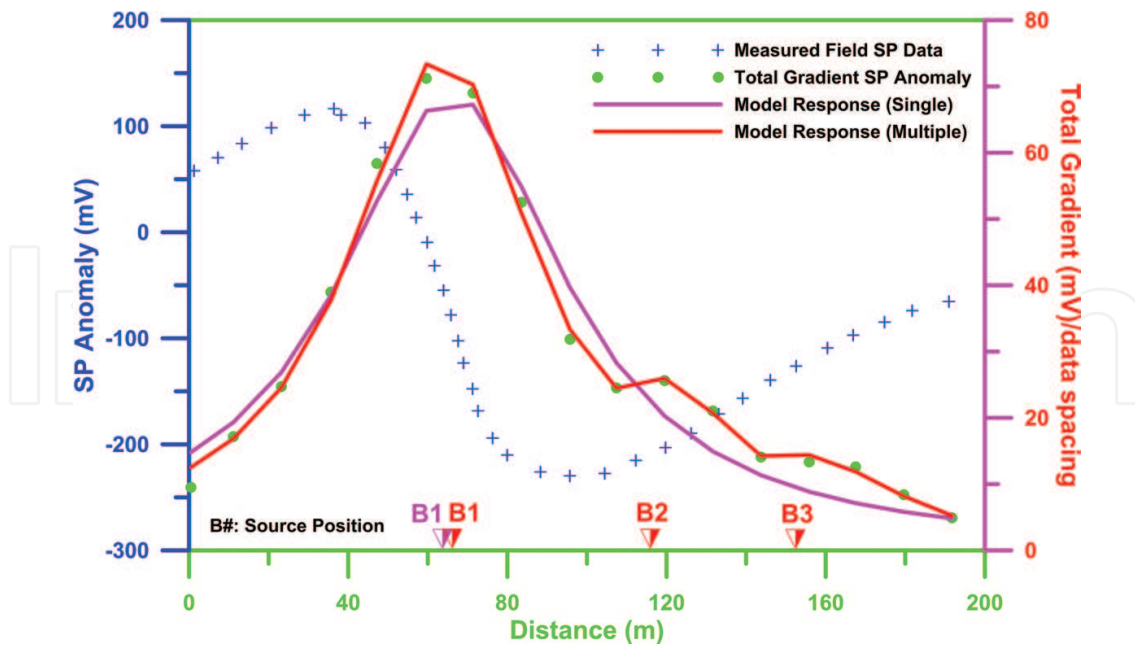
**Figure 18.** Fittings between the observed and model responses for Sulleymonkoy anomaly, Ergani, Turkey.

### 3.5.2. Senneterre area of Quebec, Canada

A total gradient of SP anomaly (**Figure 6a**) over a massive sulfide ore deposits in the Senneterre area of Quebec, Canada [97], was considered for this study. The anomaly was interpreted using enhanced local wave number technique by Srivastava and Agarwal [95] and regularized inversion by Mehanee [7] without considering TG. However, the anomaly was reinterpreted by Srivastava et al. [75] using ACO technique. Srivastava et al. [75] considered six anomalies from the TG. This anomaly was also elucidated using the present inversion method to retrieve the model parameters considering four peak anomalies, which were quite distinct. Investigation of histogram plot for multiple bodies (**Figure 19a–d**) also shows that the model parameters were precisely determined. Examination of cross-plots (**Figure 20a–d**) also shows that the appraised mean model parameters were within the ambiguity limits. The depth obtained by using the VFSA method was found to be 10.5, 4.6, 3.7, and 4.3 m, respectively. The depths obtained by Srivastava et al. [75] for the four bodies are 5, 4.2, 3.8, and 4.3 m, respectively. The assessed parameters in this study are in respectable agreement with the other work. Moreover, in the present work, all four anomalies were interpreted as multiple structures and not independently. The estimated model parameters are shown in **Table 9** along with misfit. A comparison between the observed anomaly and model responses are shown in **Figure 21**.

### 3.6. Conclusions

It is well known that the local search inversion or the optimization has faster convergence rate. However, while trying to search the global optima, it can be trapped in the local minima. Hence, selection of initial guess is very important for global optimization studies. In case of complicated structure, absence of a priori information also hampers the final solution. However, global optimization methods search the best possible solution and try to find out the exact solution
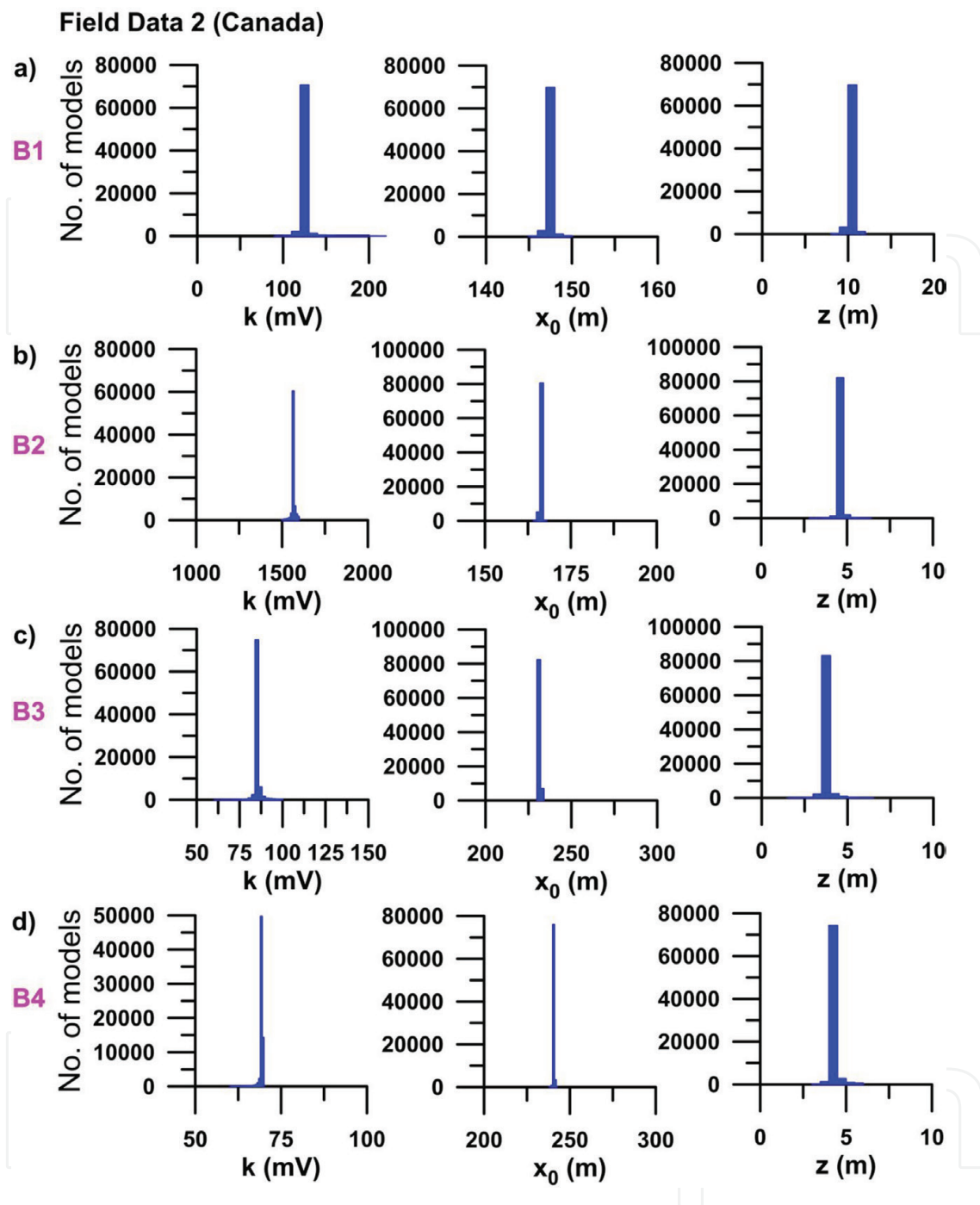
**Figure 19.** (a) Histograms of all accepted models having misfit < $10^{-2}$ for field data—single body and (b–d) histograms of all accepted models having misfit < $10^{-2}$ for field data—multiple bodies—Senneterre area of Quebec, Canada.

within a multidimensional model space. Moreover, apart from global optimization method, a statistical method can also be applied to find out the ambiguity associated with the final results.

In this study, an effort was made to examine the relevance and adequacy of VFSA on the parameter appraisals from ASA or TG of SP anomalies. In this method, the experimental studies were executed utilizing hypothetically derived data and field data. The elucidation of the amplitude coefficient, location, depth, and shape of a subsurface structure from TG
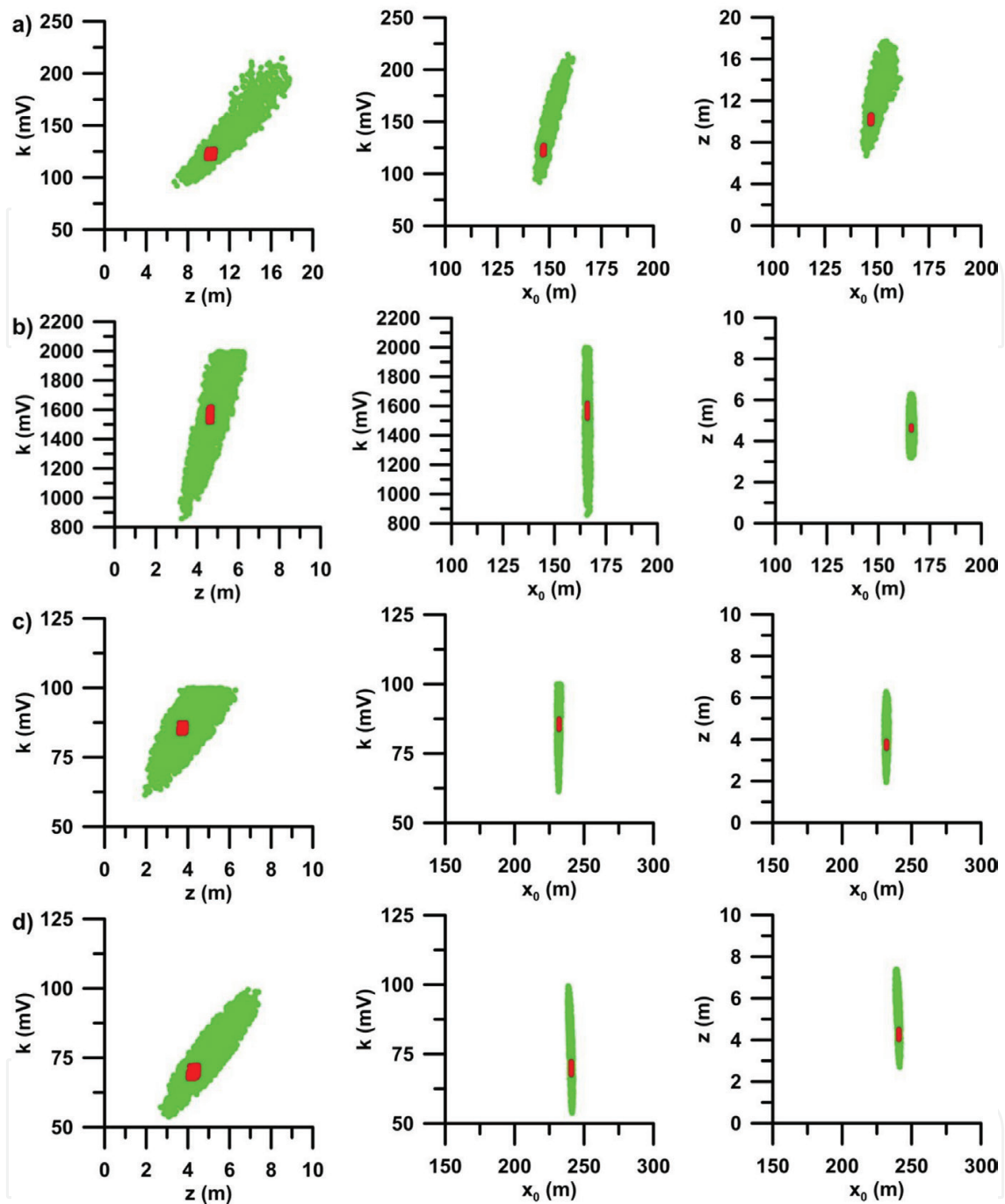
**Figure 20.** (a) Cross-plots between amplitude coefficient ($k$), depth ($z$), shape location ($x_0$) for all models having misfit < threshold ($10^{-2}$ for noise-free data) (green), and models with PDF > 60.65% (red) for field data—single body, (b–d) cross-plots between amplitude coefficient ($k$), depth ($z$), shape location ($x_0$) for all models having misfit < threshold ($10^{-2}$ for noise-free data) (green), and models with PDF > 60.65% (red) for field data—multiple bodies—Senneterre area of Quebec, Canada.

anomaly can be very much established utilizing the present technique. Synthetic data tests were performed utilizing both noise-free and noisy information sets derived from idealized geobodies. The present work reveals, while interpreting every single model parameter (amplitude coefficient, location, depth, shape) together, the VFSA method produces excellent results. Moreover, multiple model bodies were interpreted very efficiently.

| Model parameters | Search range | Present method B1 | Search range | Present method B2 | Search range | Present method B3 | Search range | Present method B4 |
|---|---|---|---|---|---|---|---|---|
| $k$ (mV) | 10–500 | 122.1 ± 0.7 | 100–2000 | 1568.4 ± 13.9 | 0–100 | 85.4 ± 0.6 | 0–100 | 69.5 ± 0.3 |
| $x_0$ (m) | 100–200 | 147.2 ± 0.1 | 100–200 | 166.1 ± 0.1 | 200–250 | 232.0 ± 0.1 | 200–250 | 240.9 ± 0.1 |
| $z$ (m) | 0–20 | 10.5 ± 0.1 | 0–10 | 4.6 ± 0.1 | 0–10 | 3.7 ± 0.1 | 0–10 | 4.3 ± 0.1 |
| $q$ | 0–2 | 0.5 | 0–2 | 1.0 | 0–2 | 0.5 | 0–2 | 0.5 |
| Misfit | | $3.6 \times 10^{-3}$ | | $2.2 \times 10^{-3}$ | | $3.4 \times 10^{-3}$ | | $5.5 \times 10^{-3}$ |

Srivastava et al. [75] (ACO) $x_0$ and $z_0$ are the coordinate of the source location in unit of data spacing (0.61 m).

| Model parameters | Search space | TGM peak 1 | Search space | TGM peak 3 | Search space | TGM peak 5 | Search space | TGM peak 6 |
|---|---|---|---|---|---|---|---|---|
| $k$ (mV) | 1–6250 | 157 ± 17 | 1–42,000 | 6998 ± 72 | 1–15,000 | 2201 ± 36 | 1–13,000 | 944 ± 11 |
| $x_0$ (m) | 220–240 | 143.2 ± 2.0 | 265–285 | 167.4 ± 2.1 | 370–390 | 231.2 ± 1.2 | 380–410 | 242.5 ± 3.1 |
| $z$ (m) | 1–50 | 5.0 ± 0.2 | 1–50 | 4.2 ± 0.2 | 1–50 | 3.8 ± 0.3 | 1–50 | 4.3 ± 0.1 |
| $\beta$ (=2$q$) | 0.2–4 | 1.3 ± 0.1 | 0.2–4 | 2.2 ± 0.3 | 0.2–4 | 2.2 ± 0.3 | 0.2–4 | 2.3 ± 0.3 |

**Table 9.** Search range and interpreted mean model for Senneterre area of Quebec, Canada.
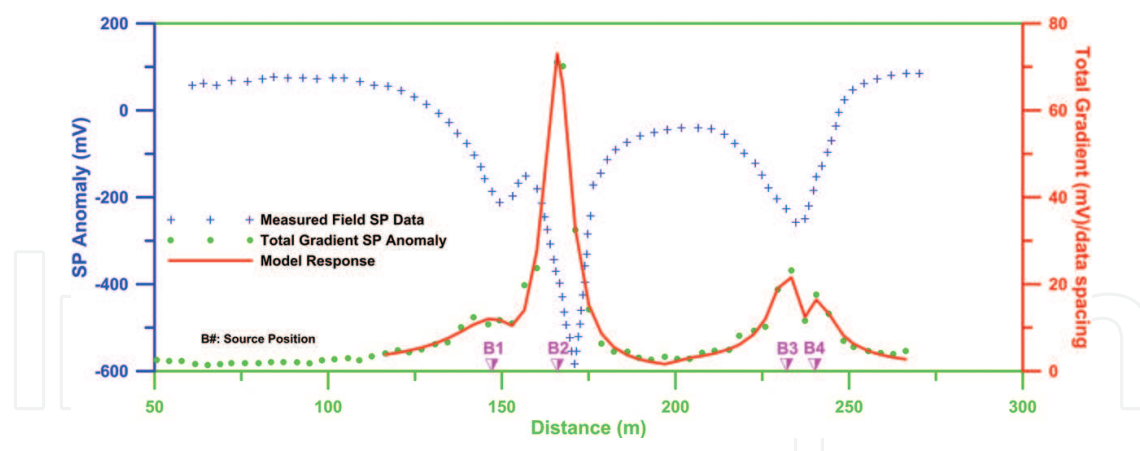
**Figure 21.** Fittings between the observed and model responses for Senneterre area of Quebec, Canada.

The subsequent histogram and cross-plots investigation proposes that the acquired parameters were within the high probability and less uncertainty. This is also supported by the rapid and stable convergence rate of the present inversion method. The viability of this approach has been effectively demonstrated employing noise-free and noisy data. The suitability of this technique for useful application in mineral investigation has been additionally shown on two field cases (Sulleymonkoy anomaly, Ergani, Turkey, Senneterre area of Quebec, Canada). The field data were presumed to be formed due to different idealized geological bodies as mentioned in the published literature. The technique can be utilized to understand numerous structures from the anomaly. The assessed inverse parameters for the field examples were observed to be in fair agreement with other alternate techniques such as PSO.

It is noteworthy to mention that the present work does not get affected by wide search range. Other studies suggested that the search range must be carried out by the workers to understand the effect of search range and the solution.

## Acknowledgements

## Author details

Arkoprovo Biswas

Address all correspondence to: arkoprovo@gmail.com

Department of Geology, Centre of Advanced Study, Institute of Science, Banaras Hindu University, Varanasi, UP, India

# References

[1]  Biswas A. A review on modeling, inversion and interpretation of self-potential in mineral exploration and tracing Paleo-shear zones. Ore Geology Reviews. 2017;**91**:21-56

[2]  Biswas A, Sharma SP. Integrated geophysical studies to elicit the structure associated with uranium mineralization around South Purulia shear zone, India: A review. Ore Geology Reviews. 2016;**72**:1307-1326

[3]  Biswas A, Sharma SP. Interpretation of self-potential anomaly over 2-D inclined thick sheet structures and analysis of uncertainty using very fast simulated annealing global optimization. Acta Geodaetica et Geophysica. 2016;**52**(4):439-455

[4]  Biswas A, Mandal A, Sharma SP, Mohanty WK. Delineation of subsurface structure using self-potential, gravity and resistivity surveys from South Purulia shear zone, India: Implication to uranium mineralization. Interpretation. 2014;**2**(2):T103-T110

[5]  Biswas A. Identification and resolution of ambiguities in interpretation of self-potential data: Analysis and integrated study around South Purulia Shear Zone, India [PhD thesis]. Department of Geology and Geophysics, Indian Institute of Technology Kharagpur; 2013. 199 pp. DOI: http://www.idr.iitkgp.ac.in/xmlui/handle/123456789/3247

[6]  Essa K, Mahanee S, Smith PD. A new inversion algorithm for estimating the best fitting parameters of some geometrically simple body to measured self-potential anomalies. Exploration Geophysics. 2008;**39**:155-163

[7]  Mehanee S. An efficient regularized inversion approach for self-potential data interpretation of ore exploration using a mix of logarithmic and non-logarithmic model parameters. Ore Geology Reviews. 2014;**57**:87-115

[8]  Sundararajan N, SrinivasaRao P, Sunitha V. An analytical method to interpret self-potential anomalies caused by 2D inclined sheets. Geophysics. 1998;**63**:1551-1555

[9]  Corry CE. Spontaneous potential associated with porphyry sulphide mineralization. Geophysics. 1985;**50**:1020-1034

[10]  Heinrichs WE. Geophysical investigation, ore knob mine, Ashe County, North Carolina. In: Hanson DA, Heinrichs WE, Holmer RC, MacDougall RE, Rogers Summer JS, Ward SH, editors. Mining Geophysics Volume 1, Case Histories. Tusla: SEG; 1966. pp. 179-184

[11]  Logn O, Bolviken B. Self-potentials at the Joma pyrite deposit. Geoexploration. 1974;**12**:11-28

[12]  Sato M, Mooney HM. The electrochemical mechanism of sulfide self-potentials. Geophysics. 1960;**25**:226-249

[13]  Mendonca CA. Forward and inverse self-potential modeling in mineral exploration. Geophysics. 2008;**73**:F33-F43

[14]  Monteiro Santos FA, Almeida EP, Castro R, Nolasco M, Mendes-Victor L. A hydrogeological investigation using EM34 and SP surveys. Earth Planets and Space. 2002;**54**:655-662

[15]  Rizzo E, Suski B, Revil A, Straface S, Troisi S. Self-potential signals associated with pumping tests experiments. Journal of Geophysical Research. 2004;**109**:B10203

[16]  Titov K, Levitski A, Konosavski PK, Tarasov AV, Ilyin YT, Bues MA. Combined application of surface geoelectrical methods for groundwater-flow modeling: A case history. Geophysics. 2005;**70**(5):H21-H31

[17]  Jardani A, Revil A, Boleve A, Dupont JP. Three-dimensional inversion of self-potential data used to constrain the pattern of groundwater flow in geothermal fields. Journal of Geophysical Research-Solid Earth. 2008;**113**:B09204

[18]  Minsley BJ, Coles DA, Vichabian Y, Morgan FD. Minimization of self-potential survey mis-ties acquired with multiple reference locations. Geophysics. 2008;**73**:F71-F81

[19]  Zlotnicki J, Nishida Y. Review on morphological insights of self-potential anomalies on volcanoes. Surveys in Geophysics. 2003;**24**:291-338

[20]  Darnet M, Marquis G. Modelling streaming potential (SP) signals induced by water movement in the vadose zone. Journal of Hydrology. 2004;**285**:114-124

[21]  Sailhac P, Darnet M, Marquis G. Electrical streaming potential measured at the ground surface: Forward modeling and inversion issues for monitoring infiltration and characterizing the vadose zone. Vadose Zone Journal. 2004;**3**:1200-1206

[22]  Hunter LE, Powers MH. Geophysical investigations of earthen dams: An overview. In: 21st EEGS Symposium on the Application of Geophysics to Engineering and Environmental Problems. Poster Overviews II. 2008. pp. 1083-1096

[23]  Jardani A, Revil A, Bolève A, Crespy A, Dupont JP, Barrash W. Tomography of the Darcy velocity from self-potential measurements. Geophysical Research Letters. 2007;**34**:1-6

[24]  Maineult A. Estimation of the electrical potential distribution along metallic casing from surface self-potential profile. Journal of Applied Geophysics. 2016;**129**:66-78

[25]  Drahor MG. Application of the self-potential method to archaeological prospection: Some case histories. Archaeological Prospection. 2004;**11**:77-105

[26]  Vichabian Y, Morgan FD. Self-potentials in cave detection. The Leading Edge. 2002; **21**:866-871

[27]  Jouniaux L, Pozzi JP. Streaming potential and permeability of saturated sandstones under triaxial stress: Consequences for electrotelluric anomalies prior to earthquakes. Journal of Geophysical Research. 1995;**100**(B6):10197-10209

[28]  Kulessa B, Hubbard B, Brown GH. Cross-coupled flow modeling of coincident streaming and electrochemical potentials and application to sub-glacial self-potential data. Journal of Geophysical Research. 2003;**108**(B8):2381

[29]  Titov K, Revil A, Konosavsky P, Straface S, Troisi S. Numerical modelling of self-potential signals associated with a pumping test experiment. Geophysical Journal International. 2005;**162**:641-650

[30] Schiavone D, Quarto R. Self-potential prospecting in the study of water movements. Geoexploration. 1984;**22**:47-58

[31] Revil A, Cary L, Fan Q, Finizola A, Trolard F. Self-potential signals associated with preferential ground water flow pathways in a buried paleo-channel. Geophysical Research Letters. 2005;**32**:L07401. DOI: 10.1029/2004GL022124

[32] Di Maio R, Patella D. Self-potential anomaly in volcanic areas: The Mt. Etna case history. Acta Vulcanologica. 1994;**4**:119-124

[33] Di Maio R, Di Sevo V, Gianmmetti S, Patella D, Piscitelli S, Silenziario C. Self-potential anomalies in some Italian volcanic areas. Annals of Geophysics. 1996;**39**:179-188

[34] Mehanee S. Tracing of paleo-shear zones by self-potential data inversion: Case studies from the KTB, Rittsteig, and Grossensees graphite-bearing fault planes. Earth, Planets and Space. 2015;**67**:14

[35] Biswas A, Sharma SP. Interpretation of self-potential anomaly over idealized body and analysis of ambiguity using very fast simulated annealing global optimization. Near Surface Geophysics. 2015;**13**(2):179-195

[36] Biswas A, Sharma SP. Resolution of multiple sheet-type structures in self-potential measurement. Journal of Earth System Science. 2014;**123**(4):809-825

[37] Biswas A, Sharma SP. Optimization of self-potential interpretation of 2-D inclined sheet-type structures based on very fast simulated annealing and analysis of ambiguity. Journal of Applied Geophysics. 2014;**105**:235-247

[38] El-Araby HM. A new method for complete quantitative interpretation of self-potential anomalies. Journal of Applied Geophysics. 2004;**55**:211-224

[39] Eppelbaum L, Khesin B, Itkis S, Ben-Avraham Z. Advanced analysis of self-potential data in ore deposits and archaeological sites. Near surface geoscience. In: 10th European Meeting of Environmental and Engineering Geophysics. Utrecht, The Netherlands; 2004. pp. 1-4

[40] Mehanee S, Essa KS, Smith PD. A rapid technique for estimating the depth and width of a two-dimensional plate from self-potential data. Journal of Geophysics and Engineering. 2011;**8**:447-456

[41] Meiser P. A method of quantitative interpretation of self-potential measurements. Geophysical Prospecting. 1962;**10**:203-218

[42] Murthy BVS, Haricharan P. Nomograms for the complete interpretation of spontaneous potential profiles over sheet like and cylindrical 2D structures. Geophysics. 1985;**50**:1127-1135

[43] Paul MK. Direct interpretation of self-potential anomalies caused by inclined sheets of infinite extension. Geophysics. 1965;**30**:418-423

[44] Pekşen E, Yas T, Kayman YA, Őzkan C. Application of particle swarm optimization on self-potential data. Journal of Applied Geophysics. 2011;**75**:305-318

[45] Rao AD, Babu RHV. Quantitative interpretation of self-potential anomalies due to two-dimensional sheet-like bodies. Geophysics. 1983;**48**:1659-1664

[46] Rao AD, Babu H, Sivakumar Sinha GD. A Fourier transform method for the interpretation of self-potential anomalies due to two-dimensional inclined sheet of finite depth extent. Pure and Applied Geophysics. 1982;**120**:365-374

[47] Roy A, Chowdhury DK. Interpretation of self-potential data for tabular bodies. Journal of Scientific and Engineering Research. 1959;**3**:35-54

[48] Abdelrahman EM, Saber HS, Essa KS, Fouad MA. A least-squares approach to depth determination from numerical horizontal self-potential gradients. Pure and Applied Geophysics. 2004;**161**:399-411

[49] El-Kaliouby HM, Al-Garani MA. Inversion of self-potential anomalies caused by 2D inclined sheets using neural networks. Journal of Geophysics and Engineering. 2009;**6**:29-34

[50] Jagannadha RS, Rama RP, Radhakrishna MIV. Automatic inversion of self-potential anomalies of sheet-like bodies. Computers and Geosciences. 1993;**19**:61-73

[51] Murthy IVR, Sudhakar KS, Rao PR. A new method of interpreting self- potential anomalies of two-dimensional inclined sheets. Computers and Geosciences. 2005;**31**:661-665

[52] Tlas M, Asfahani J. A best-estimate approach for determining self-potential parameters related to simple geometric shaped structures. Pure and Applied Geophysics. 2007;**164**:2313-2328

[53] Tlas M, Asfahani J. An approach for interpretation of self-potential anomalies due to simple geometrical structures using flair function minimization. Pure and Applied Geophysics. 2013;**170**:895-905

[54] Babu HVR, Rao DA. A rapid graphical method for the interpretation of the self-potential anomaly over a two-dimensional inclined sheet of finite depth extent. Geophysics. 1988;**53**:1126-1128

[55] Murthy BVS, Haricharan P. Self-potential anomaly over double line of poles—Interpretation through log curves. Proceedings of the Indian Academy of Science (Earth and Planetary Science). 1984;**93**:437-445

[56] Rao BSR, Murthy IVR, Reddy SJ. Interpretation of self-potential anomalies of some simple geometrical bodies. Pure and Applied Geophysics. 1970;**78**:60-77

[57] Abdelrahman EM, Essa KS, Abo-Ezz ER, Sultan M, Sauck WA, Gharieb AG. New least-square algorithm for model parameters estimation using self- potential anomalies. Computers and Geosciences. 2008;**34**:1569-1576

[58] Roy SVS, Mohan NL. Spectral interpretation of self-potential anomalies of some simple geometric bodies. Pure and Applied Geophysics. 1984;**78**:66-77

[59] Patella D. Introduction to ground surface self-potential tomography. Geophysical Prospecting. 1997;**45**(4):653-681

[60] Patella D. Self-potential global tomography including topographic effects. Geophysical Prospecting. 1997;**45**:843-863

[61] Abdelrahman EM, El-Araby HM, Hassanein AG, Hafez MA. New methods for shape and depth determinations from SP data. Geophysics. 2003;**68**:1202-1210

[62] Abdelrahman EM, El-Araby TM, Essa KS. Shape and depth determinations from second moving average residual self-potential anomalies. Journal of Geophysics and Engineering. 2009;**6**:43-52

[63] Monteiro Santos FA. Inversion of self-potential of idealized bodies anomalies using particle swarm optimization. Computers and Geosciences. 2010;**36**:1185-1190

[64] Fedi M, Abbas MA. A fast interpretation of self-potential data using the depth from extreme points method. Geophysics. 2013;**78**:E107-E116

[65] Li X, Yin M. Application of differential evolution algorithm on self-potential data. PLoS One. 2012;**7**(12):e51199

[66] Di Maio R, Piegari E, Rani P, Avella A. Self-potential data inversion through the integration of spectral analysis and tomographic approaches. Geophysical Journal International. 2016;**206**:1204-1220

[67] Di Maio R, Rani P, Piegari E, Milano L. Self-potential data inversion through a genetic-Price algorithm. Computers and Geosciences. 2016;**94**:86-95

[68] Essa K, El-Hussein M. A new approach for the interpretation of self-potential data by 2-D inclined plate. Journal of Applied Geophysics. 2017;**136**:455-461

[69] Di Maio R, Piegari E, Rani P. Source depth estimation of self-potential anomalies by spectral methods. Journal of Applied Geophysics. 2017;**136**:315-325

[70] Srivastava S, Agarwal BNP. Inversion of the amplitude of the two-dimensional analytic signal of magnetic anomaly by the particle swarm optimization technique. Geophysical Journal International. 2010;**182**:652-662

[71] Nabighian MN. The analytic signal of two-dimensional magnetic bodies with polygonal cross-section, its properties and use for automated anomaly interpretation. Geophysics. 1972;**37**:507-517

[72] Nabighian MN, Grauch VJS, Hansen RO, LaFehr TR, Li Y, Peirce JW, et al. 75th anniversary. The historical development of the magnetic method in exploration. Geophysics. 2005;**70**:33ND-61ND

[73]  Nabighian M N, Ander M E, Grauch V JS, Hansen R O, LaFehr T R, Li Y, et al. 75th anniversary. The historical development of the gravity method in exploration. Geophysics. 2005;**70**:63ND-89ND

[74]  Nettleton LL. Elementary Gravity and Magnetic for Geologists and Seismologists. Tulsa, OK: SEG; 1971

[75]  Srivastava S, Datta D, Agarwal BNP, Mehta S. Applications of ant colony optimization in determination of source parameters from total gradient of potential fields. Near Surface Geophysics. 2014;**12**:373-389

[76]  Ingber L, Rosen B. Genetic algorithms and very fast simulated reannealing: A comparison. Mathematical and Computer Modeling. 1992;**16**(11):87-100

[77]  Sen MK, Stoffa PL. Global Optimization Methods in Geophysical Inversion. 2nd ed. London: Cambridge Publisher; 2013

[78]  Sharma SP, Biswas A. Interpretation of self-potential anomaly over 2D inclined structure using very fast simulated annealing global optimization—An insight about ambiguity. Geophysics. 2013;**78**(3):WB3-W15

[79]  Biswas A. Interpretation of gravity and magnetic anomaly over thin sheet-type structure using very fast simulated annealing global optimization technique. Modeling Earth Systems and Environment. 2016;**2**(1):30

[80]  Biswas A. A comparative performance of least square method and Very fast simulated annealing global optimization method for interpretation of self-potential anomaly over 2-D inclined sheet type structure. Journal of the Geological Society of India. 2016;**88**(4):493-502

[81]  Biswas A, Parija MP, Kumar S. Global nonlinear optimization for the interpretation of source parameters from total gradient of gravity and magnetic anomalies caused by thin dyke. Annals of Geophysics. 2017;**60**(2):G0218, 1-17

[82]  Biswas A. Interpretation of residual gravity anomaly caused by a simple shaped body using very fast simulated annealing global optimization. Geoscience Frontiers. 2015;**6**(6):875-893

[83]  Dosso SE, Oldenburg DW. Magnetotelluric appraisal using simulated annealing. Geophysical Journal International. 1991;**106**:370-385

[84]  Rothman DH. Nonlinear inversion, statistical mechanics and residual statics estimation. Geophysics. 1985;**50**:2784-2796

[85]  Rothman DH. Automatic estimation of large residual statics correction. Geophysics. 1986;**51**:337-346

[86]  Sharma SP. VFSARES—A very fast simulated annealing FORTRAN program for interpretation of 1-D DC resistivity sounding data from various electrode array. Computers and Geosciences. 2012;**42**:177-188

[87] Biswas A. Inversion of source parameters from magnetic anomalies for mineral /ore deposits exploration using global optimization technique and analysis of uncertainty. Natural Resources Research. 2018;**27**(1):77-107

[88] Biswas A, Acharya T. A Very Fast Simulated Annealing (VFSA) method for inversion of magnetic anomaly over semi-infinite vertical rod-type structure. Modeling Earth Systems and Environment. 2016;**2**(4):198

[89] Mosegaard K, Tarantola A. Monte Carlo sampling of solutions to inverse problems. Journal of Geophysical Research. 1995;**100**(B7):12431-12447

[90] Sen MK, Stoffa PL. Bayesian inference, Gibbs sampler and uncertainty estimation in geophysical inversion. Geophysical Prospecting. 1996;**44**:313-350

[91] Yungul S. Interpretation of spontaneous polarization anomalies caused by spherical ore bodies. Geophysics. 1950;**15**:237-246

[92] Agarwal BNP. Quantitative interpretation of self-potential anomalies. In: Expanded Abstract Volume of the 54th SEG Annual Meeting and Exposition; Atlanta. 1984. pp. 154-157

[93] Agarwal B, Srivastava S. Analyses of self-potential anomalies by conventional and extended Euler deconvolution techniques. Computers and Geosciences. 2009;**35**:2231-2238

[94] Bhattacharya BB, Roy N. A note on the use of nomograms for self-potential anomalies. Geophysical Prospecting. 1981;**29**:102-107

[95] Srivastava S, Agarwal BNP. Interpretation of self-potential anomalies by enhanced local wave number technique. Journal of Applied Geophysics. 2009;**68**:259-268

[96] Sundararajan N, Srinivas Y. A modified Hilbert transform and its application to self-potential interpretation. Journal of Applied Geophysics. 1996;**36**:137-143

[97] Telford WM, Geldart LP, Sheriff RE. Applied Geophysics. London: Cambridge University Press; 1990